A Thesis
entitled

Radial Velocity Variations in ι Herculis

by

Christopher L. Mulliss

As partial fulfillment of the requirements for
the Master of Science Degree in
Physics

Advisor : Dr. N. D. Morrison

Graduate School

The University of Toledo
(March 1996)

An Abstract of

Radial Velocity Variations in ι Herculis

Christopher L. Mulliss

Submitted in partial fulfillment
of the requirements for the
Master of Science Degree in Physics

The University of Toledo
(March 1996)

The radial velocity of S II (6) 5453.810Å has been measured in 58 high–resolution spectra of the B3 IV star ι Herculis which undergoes both orbital and pulsational velocity variations. An iterative process was used to determine the orbit which separated the orbital and pulsational variations, allowing a separate least–squares solution for each. The analysis has yielded a new estimate of the orbital elements.

The pulsational properties & their time evolution were studied by taking Lomb periodograms of 30–point "windows" of the orbit residuals and then fitting a Fourier–harmonic series to the dominant period for each window. A previously unreported 0.80d variation dominated the residuals early in the observations. Two periods observed by Rogerson (1984) and their predicted beat period dominated the residuals late in the observations. Most importantly, the amplitude of the 0.80d mode gradually decreased until the role of dominant mode was taken over by the Rogerson beat period whose amplitude gradually increased during the later part of the observations. Evidence that this mode switching may be caused by tidal interactions at periastron is presented.

Acknowledgments

I would like to thank the following people for their assistance in observing ι Herculis: Dr. N. D. Morrison, Jason Aufdenberg, Karl Gordon, Michelle Beaver, and Partick Oeullette. I would also like to thank Dr. Bernard Bopp for making the orbit determination program available to me. I thank Dr. Nancy Morrison for her guidance and advice throughout this project. I thank the members of my thesis committee (Drs. Ellis and Anderson) for their many useful comments and suggestions. I would like to recognize Mr. Robert Burmeister for his work as telescope technician. This research has made use of the SIMBAD astronomical database operated at the CDS in Strasbourg, France. Support for observational research at Ritter Observatory is provided by The University of Toledo and by NSF grant AST–9024802 to B. W. Bopp.

Contents

List of Figures

List of Tables

Chapter 1

Introduction

Iota Herculis is a well–studied B3 IV star that exhibits a wide variety of periodic behavior on at least three time scales: a 112-day radial velocity variation due to its motion in a binary orbit; pulsational variations in radial velocities, photometry, line profiles, and line strengths with periods on the order of hours and longer periods on the order of one to a few days.

Table 1 lists variations that have been noted in ι Herculis by previous (but recently published) researchers. In this table, many different observable quantities were used to detect variability including: line profiles (LP), radial velocity (RV), equivalent widths (W_λ), and photometry (Phot).

There are many reasons why ι Her is a well studied star. Because it is a sharp–lined B–type star, line blending is not a serious problem. For this reason, ι Her is often used as an abundance standard in differential abundance analyses. The fact that it is a sharp–lined star also makes radial velocity measurements very precise. Iota Her is situated on the HR diagram in a strip of temperatures and luminosities where pulsational instabilities are known to occur. This instability strip contains at

Table 1: Variability in ι Her

Type	Variability Index	Period(s)	Reference
RV	Balmer Hβ to H–15	112.7175 days	Kodaira 1971
LP	Si III λ4568	0.208, 0.413, & 0.579 days	Smith 1978
RV	He I $\lambda\lambda$3819, 4009, 4026, 4143, 4387, & 4471	113.804 days	Abt & Levy 1978
W_λ	P II λ4127.57 Ar II $\lambda\lambda$4128.4 & 4131.73 Cl II λ4132.48	1 or 2 days 40 minutes – 2 hours Few hours	Smith 1981
RV	Fe III λ1096.606	1.515 & 1.618 days	Rogerson, 1984
Phot	UV filter*	0.12 or 0.14 days	Chapellier *et al.* 1987
RV	Si II $\lambda\lambda$4128 & 4131	1.43 or 3.33 days	Mathias & Waelkens 1995

* Bandpass 100Å, Central Wavelength 3500Å, Sareyan *et al.* 1976

least two classes of pulsating stars of which ι Her may be a member; these classes are the β Cep class and the 53 Per class (and the related Slowly Pulsating class of B–type stars (SPB)). The β Cep stars are late O–type to early B–type stars that pulsate predominantly in radial modes with periods that range from 0.1 days to 0.3 days, although many are known to have non–radial pulsation modes as well (Unno *et al.* 1989; Moskalik 1995). Radial pulsations are accompanied by variations in the temperature and pressure of the star's entire atmosphere; the result is variations in light, color, line widths and line strengths, and large–amplitude variations in radial velocity (Cox 1980).

The 53 Per stars surround the β Cep stars in the instability strip, having spectral types that range from late O–type to middle B–type; these stars are classified from line profile variations that arise from non–radial modes with periods that range from 0.5 days to 4.1 days (Cox 1980; Moskalik 1995). The SPB stars display pulsational characteristics very similar to the 53 Per stars; they differ in that they are classified by photometric variations and tend to be mid B–type stars (Waelkens 1991). Non–radial pulsations are accompanied by relatively small variations in temperature and pressure; the result is variations in line profiles that lead to small–amplitude variations in radial velocity (of line centroids) as well as light and/or color variations (Cox 1980).

Radial and non-radial pulsations have characteristically different periods because they arise from different restoring forces; radial pulsation modes have pressure forces as the restoring force whereas non–radial modes have the relatively weak force of buoyancy as a restoring force. The strength of the pressure and buoyancy forces in the stars in the instability strip determine the characteristic periods of the radial and non–radial pulsation modes according to theoretical models; pulsation periods of 0.1 to 0.3 days imply radial β Cepei–type pulsation while pulsation periods of 0.5 to 4.1 days imply non–radial 53 Per–type pulsation. In stars that undergo non–radial pulsations, stellar rotation can cause pulsation modes to occur in groups of closely spaced periods. Two of these periods can beat to produce a variation that is much longer than 4.1 days (Unno *et al.* 1989). Because radial pulsation modes are not affected in this way by rotation and are therefore always widely separated in frequency, any variations with periods longer than 4.1 days that can be attributed to beating necessarily point toward non–radial pulsations.

Table 1 demonstrates that both time scales (and therefore both types of pulsations) have been observed in ι Her. Table 1 also shows that there is a general lack of agreement among different investigators as to what period best describes variations in this star. The lack of agreement may be due to the fact that ι Her (like many β Cep and 53 Per stars) can display multiperiodic behavior where several pulsational periods are observed at the same time. Multiperiodic behavior may also take the form of mode switching where different modes are active at different times. Such behavior may contribute to the disagreement seen in Table 1.

The purpose of this work is to classify pulsation periods of ι Her in a homogeneous set of radial velocity observations taken over a long timebase. The long baseline enables the orbit to be determined and its effects subtracted from the data so that the pulsational properties can be studied. The long baseline also provides the opportunity to identify non–radial pulsation periods through direct detection and/or the detection of their beat periods. The observations in this work also enable the detection of short–period, β Cep–type, radial pulsations, should they be strongly present in the data. An extreme definition of the β Cep class states that a radial mode (i.e. short–period) pulsation must be dominant (Sterken & Jerzykiewicz 1990). Short–period variations may have been observed in ι Her with the photometry of Chapellier *et al.* (1987) and are suggested by the radial velocity work of Mathias & Waelkens (1995). Because radial pulsations typically yield larger amplitude radial velocity variations than non–radial pulsations and because the present data set is of high enough quality to detect (at least) the dominant pulsation mode, this work will be able to determine whether ι Her belongs to the β Cep class of stars as so defined. A careful examination of a star such as ι Her may clarify the relationships between the β Cep, 53 Per, and SPB classes of pulsating B–type stars. A better understanding of stellar pulsations will ultimately lead to a deeper understanding of the internal structure of stars.

Another purpose of this work is to examine the multiperiodic behavior of ι Her. The data will be examined for evidence that more than one pulsation mode is active at a given time as well as for signs of mode switching, in which the role of dominant pulsation mode is passed between two different pulsation modes. Pulsation modes will also examined for changes in radial velocity amplitude.

Chapter 2

Observations

Fifty–eight high–resolution CCD échelle spectra have been obtained of ι Her with the 1–m telescope of Ritter Observatory along with 25 spectra of radial velocity standards. These observations were obtained from February 2, 1994 through March 11, 1995. The data consist of single observations (1 spectrum per night) as well as many series of spectra taken consecutively over several hours.

The spectral resolution of the observations is determined by the width of the spectrograph's entrance slit. All observations used the 'standard' wide slit; the sacrifice of spectral resolution was made to increase throughput and shorten exposure times. This choice of slit width gives an instrument function with a FWHM of 4.2 pixels (0.23Å) at 5875Å which corresponds to a resolving power of R = 26,000.

The observations were obtained in two different wavelength regions of the optical spectrum. The 26 "blue" observations contain 15 partial échelle orders surrounding Hβ; each has a spectral coverage of about 50Å and is separated from adjacent partial orders by about 50Å. The 32 "red" observations contain 9 partial échelle orders surrounding Hα; each has a spectral coverage of about 70Å and is separated from adjacent partial orders by about 90Å.

Because the quantum efficiency of the CCD chip and the transmission of the fiber optic cable are much larger in the red than in the blue, the observations in these two regions have different characteristic exposure times. Table 2 shows the characteristics of the blue and red observations as well as the combined average properties (weighted by the number of observations in each region).

Table 2: Properties of the Observations

Property	Blue Obs	Red Obs	Blue + Red Obs.
Exposure Times (sec)	1200 – 2400	300 – 1800	300 – 2400
Ave Exposure Time (sec)	1550	950	1200
SNR (Range)	50 – 100	100 – 150	50 – 150
Average SNR	75	125	100

The spectroscopic observations were reduced using standard routines from IRAF (Image Reduction and Analysis Facility) Version 2.10.3 Beta.[1] The spectra were corrected for the bias voltage on each pixel of the CCD chip, flat–fielded to remove pixel–to–pixel sensitivity variations, and wavelength–calibrated as described below. The light from the calibration lamps used in the reduction of the data travels the same optical path through the fiber and the spectrograph as does the light from stars.

The bias voltage pattern on the CCD chip was estimated by taking 5–10 “bias” frames during each night of observing. These spectra are near–zero length exposures

---

[1] IRAF is distributed by the National Optical Astronomy Observatories, which are operated by the Association of Universities for Research in Astronomy, Inc., under contract with the National Science Foundation.

taken with no light falling on the CCD. The bias exposures are averaged to eliminate the effects of readout noise. The average bias is subtracted from all other exposures.

During each night of observing, 5–10 “flat” frames were taken; the flat spectra are exposures of a nearly continuous–spectrum lamp. The flat lamp has a spectral energy distribution that varies slowly so that when the light is dispersed onto the CCD chip, the illumination around each pixel approximates a flat source of radiation. In this way, the photoelectron count at each pixel can be compared to its neighboring pixels to determine pixel–to–pixel sensitivity variations; these variations are then divided out of the stellar spectra. The flat exposures are also used to locate where the échelle orders lie on the CCD chip.

Finally, the stellar spectra were wavelength calibrated by taking comparison spectra throughout each night of observing, often directly before and after each stellar exposure. A comparison spectrum is an exposure of light from a Th–Ar gas discharge lamp. Because the pattern of emission lines and their wavelengths are known, the comparison spectra can be used to assign a wavelength value to each pixel on the CCD chip. Because small displacements of the CCD chip within the system can cause the spectrum to shift with respect to the pixel coordinates on the CCD chip, many comparison spectra are taken during each night of observing. For each stellar spectrum, an average comparison spectrum is formed by taking a weighted time average of comparison spectra that surround the time of the stellar observation. For each stellar spectrum, a wavelength callibration is obtained from fitting the known wavelengths of Th–Ar lines to the observed pattern of lines in the average comparison spectrum. The rms deviation between the known wavelengths and those in the average comparison spectra is typically between 0.001 – 0.005 Å.

Tables 3 and 4 list the observations. The heliocentric Julian date corresponds to the number of days that have passed since UT time 12:00 on the first day of the year 4713 B.C., where 'heliocentric' refers to a quantity as it would be measured by an observer at the barycenter of the solar system. For the remainder of this work, HJD is understood to be a "reduced" date equal to the HJD at mid exposure minus 2,449,000. VHELIO is an additive correction term that converts the observed radial velocities to heliocentric radial velocities (HRV). The HJD's and VHELIO correction terms for each observation were computed using the IRAF routine RVCORRECT.

Table 3: Observations in the Blue Region

HJD	VHELIO (km s^{-1})	Exp Time (sec)	Image No.	Observer(s)
531.6722	− 2.86	1200	940628.006	KG
533.6473	− 3.17	1200	940630.009	KG, MB
564.5899	− 7.71	2400	940731.009	NDM, MB
564.6800	− 7.86	1800	940731.013	NDM, MB
564.7043	− 7.89	1800	940731.015	NDM, MB
564.7286	− 7.93	1800	940731.017	NDM, MB
564.7530	− 7.95	1200	940731.019	NDM, MB
564.7711	− 7.97	1800	940731.021	NDM, MB
581.5824	− 9.45	1200	940817.007	CLM
581.6024	− 9.48	1200	940817.009	CLM
581.6204	− 9.51	1200	940817.011	CLM
581.6386	− 9.53	1200	940817.013	CLM
581.6579	− 9.56	1200	940817.015	CLM
581.6947	− 9.61	1200	940817.019	CLM
603.5936	−10.58	1800	940908.007	CLM
603.6183	−10.61	1800	940908.009	CLM
603.6427	−10.63	1800	940908.011	CLM
603.6907	−10.67	1800	940908.015	CLM
625.5192	−10.14	1800	940930.012	CLM, PO
625.5432	−10.17	1800	940930.014	CLM, PO
625.5670	−10.20	1800	940930.016	CLM, PO
625.5906	−10.22	1800	940930.018	CLM, PO
625.6147	−10.24	1800	940930.020	CLM, PO
625.6405	−10.25	1800	940930.022	CLM, PO
653.5462	−7.67	1800	941028.014	CLM
653.5690	−7.68	1800	941028.016	CLM

Observers were CLM=Christopher L. Mulliss, NDM=Dr. N. D. Morrison
KG=Karl Gordon, MB=Michelle Beaver, and PO=Patrick Ouellette

The ability of the observations to detect periodic variations in ι Her is determined by two time scales: the exposure times and the intervals between observations. The exposure times range from 300s (0.003d) to 2400s (0.028d) with an average of 1200s (0.014d). The average exposure time is only about 14% of the

Table 4: Observations in the Red Region

HJD	VHELIO (km s^{-1})	Exp Time (sec)	Image No.	Observer(s)
389.9589	9.15	1800	940206.026	CLM
444.8891	9.88	1200	940402.026	CLM
485.7911	5.00	600	940513.018	JA
490.7673	4.21	900	940518.022	KG
490.7784	4.19	900	940518.020	KG
491.7902	4.00	900	940519.024	KG
492.7008	3.97	900	940520.018	CLM
493.7967	3.65	900	940521.027	CLM
495.7611	3.37	1200	940523.005	JA
500.7418	2.54	900	940528.017	CLM
501.7119	2.41	600	940529.007	NDM
501.7201	2.39	600	940529.008	NDM
501.7293	2.38	600	940529.009	NDM
506.7050	1.53	1200	940603.015	CLM
510.7306	0.77	1200	940607.019	NDM
510.7469	0.74	1200	940607.020	NDM
512.6654	0.51	1200	940609.016	KG
513.7287	0.23	300	940610.009	JA
514.6642	0.15	600	940611.013	CLM, PO
534.6291	– 3.31	1200	940701.014	JA, MB
544.6914	– 5.06	600	940711.027	JA
574.7255	– 9.02	1200	940811.014	CLM
594.7509	–10.44	900	940830.026	KG
594.7644	–10.44	900	940830.028	KG
599.5956	–10.48	1200	940904.016	NDM
599.6268	–10.52	600	940904.020	NDM
599.6804	–10.58	900	940904.024	NDM
613.5981	–10.60	1200	940918.012	NDM
667.5150	– 5.65	1200	941111.016	PO
778.9597	10.60	900	950303.038	KG
779.8612	10.73	900	950304.043	CLM
786.9398	10.71	1200	950311.008	CLM

Observers were CLM=Christopher L. Mulliss, NDM=Dr. N. D. Morrison JA=Jason Aufdenberg, KG=Karl Gordon, MB=Michelle Beaver, and and PO=Patrick Ouellette

minimum pulsation period (about 0.1d) that can be expected from pulsations in early B-type stars (see Chapter 1). Thus the exposure times do not inhibit the detection of even the shortest–period variations expected due to pulsations. The interval between adjacent observations spans a large range: 0.008d to 111.445d. The average interval is 6.965d, but this is heavily weighted by several large gaps in the data. Not including the three largest gaps in the data, the interval reduces to only 3.515d; this indicates that the data set is well suited to detecting variations with periods on the order of days or longer. The data are also well suited to observe variations that occur on shorter time scales because 36 of the 58 observations were taken in series and the average interval between these observations is only 0.026d. In general, then, the data set is well suited to detect variations on the time scale expected for radial pulsations and the longer periods that result from non-radial pulsations and their beat periods.

Chapter 3

Measurements

1. Line Identifications

The first step in the analysis of the spectra was to identify as many absorption features as possible. The line identifications were done by means of an interactive IDL routine.

The identifications were based on 3 criteria. All wavelengths in the line list are from C. Moore (1959) unless otherwise stated.

(1) All correctly identified lines should yield the same radial velocity in a given spectrum if one assumes that all absorption features are photospheric and that they are more or less co–moving at all times. In practice, the radial velocities from various identified absorption lines within a given spectrum had a standard deviation about their mean of 0.5 km s^{-1} or less, a value that is comparable to the observational error estimate given in Section 2.3 below.

(2) If the identification of an absorption feature is correct, then other lines of comparable or greater strength from the same multiplet should also be present in the spectrum.

(3) For as many lines as possible, additional sources of verification were sought in the literature for each line identification.

Tables 5 and 6 list the line identifications in the blue and red spectra. Lines were included in the table that were relatively unblended, strong enough to be seen through noise and blends in the continuum, and whose identification is fairly certain in this author's opinion. If no verification is given, the identification is based only on criteria (1) and (2).

The red and blue spectra overlap in a small wavelength region, in which lies a relatively strong line of S II (6) at a rest wavelength of 5453.810Å. This line is plotted in Figure 1. Because this particular line provides a baseline which includes approximately twice as many observations as lines that appear in the red or blue observations only, it was the focus of this project.

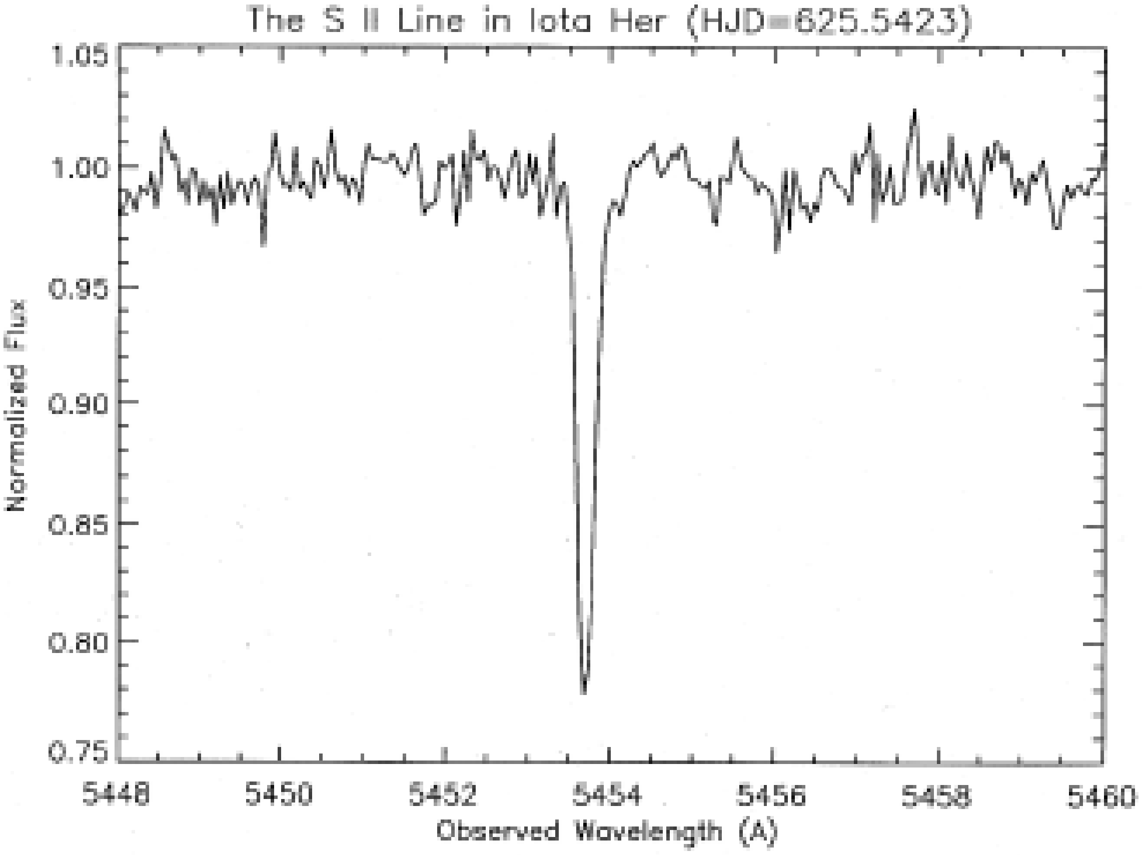

Fig. 1.— The S II (6) λ5454 line in the blue observation at HJD 625.5432.

Table 5: Blue Line Identifications

	Line Identification		
Line No.	Species	Wavelength(Å)	Verification(s)
1	Si II (3)	4130.884	[K]
2	He I (53)	4143.759	[K]
3	S II (44)	4153.098	(K)
4	S II (44)	4162.698	[P],(K)
5	O II (19)	4169.230	(K)
6	S II (49)	4294.432	(K)
7	He I (51)	4387.928	
8	O II (26)	4395.950	[P],[K]
9	O II (5)	4414.909	[P],[K]
10	O II (5)	4416.975	[P],(K)
11	He I (14)	4471.583	
12	Mg II (4)	4481.230	(P),(K)
13	N II (58)	4552.527	(K)
14	Si III (2)	4567.823	[P],[K]
15	Si III (2)	4574.759	[P],[K]
16	O II (1)	4649.139	[P],[K]
17	H I (1)	4861.332	
18	S II (7)	4991.940	
19	N II (19)	5005.140	[K]
20	S II (7)	5103.300	
21	S II (39)	5201.160	[P]
22	S II (39)	5212.610	
23	S II (38)	5320.700	
24	S II (38)	5345.670	
25	S II (6)	5453.810	[PA]
26	S II (6)	5473.590	

( ) = Blended, [ ] = Not blended

K=Kilian *et al.* 1991, P=Pintado & Adelman 1993, M=Moore 1959, and PA=Peters & Aller 1970

Line No. 3) Possibly blended with O II (19) λ4153.302.

Line No. 5) Blended with He I λ4169.0 according to K.

Line No. 11) Blend of He I (14) $\lambda\lambda$4471.477 & 4471.688; average used.

Line No. 12) Blend of Mg II (4) $\lambda\lambda$4481.129 & 4481.327; following P, the average wavelength of 4481.23Å is used.

Line No. 13) Blended with Si III (2) λ4552.616 according to K.

Line No. 14) M gives wavelength of 4567.872Å but K give 4567.823Å. The wavelength of K is used.

Line No. 15) M gives wavelength 4574.777Å but K give 4574.759Å. The wavelength of K is used.

Line No. 21) Blend of S II (39) $\lambda\lambda$5201.000 & 5201.320; average used.

Table 6: Red Line Identifications

	Line Identification		
Line No.	Species	Wavelength(Å)	Verification(s)
1	S II (6)	5428.640	[PA]
2	S II (6)	5432.770	[PA]
3	S II (6)	5453.810	[PA]
4	S II (6)	5564.940	[PA]
5	S II (11)	5578.850	
6	S II (11)	5606.110	[PA]
7	Si III (4)	5739.762	[PA]
8	He I (11)	5875.752	
9	Si II (2)	6347.091	[PA]
10	Si II (2)	6371.359	[PA]
11	Ne I (3)	6382.991	[PA]
12	Ne I (1)	6402.245	[PA]
13	H I (1)	6562.817	
14	C II (2)	6578.030	[PA]
15	C II (2)	6582.850	[PA]

( ) = Blended, [ ] = Not blended

M=Moore 1959, PA=Peters & Aller 1970

Line No. 7) PA give a wavelength of 5739.73Å but M gives 5739.762Å. The wavelength of M is used.

Line No. 8) Blend of He I (11) $\lambda\lambda\lambda$5875.618, 5875.650, & 5875.989; average used.

Line No. 9) PA give a wavelength of 6347.10Å, but M gives 6347.091Å. The wavelength of M is used.

2. Radial Velocity Measurements

2.1. Description of the Method

All wavelength measurements that are used in this paper correspond to the wavelength where a fitted absorption line profile has its minimum flux. The measurements were made using a graphically interactive IDL routine in the following manner. The user estimates the wavelength that corresponds to the minimum of an absorption line by pointing a cursor at a plot of the spectrum. The wavelength values of the two data points that surround the cursor position are averaged to give W_o. To a user–specified number of data points to the right and left of W_o, a polynomial of the following form is then fitted:

$$F_n = \mathrm{a} + \mathrm{b}\ (\mathrm{W}–W_o)+\mathrm{c}\ (\mathrm{W}–W_o)^2$$

where F_n is the continuum normalized flux and W is the wavelength in angstroms.

The user then may adjust how many data points on each side of W_o are included in the polynomial fit. When the user is satisfied with the fit, the minimum of the fitted polynomial is found; this value is taken as the observed wavelength of the line. In practice at least 5 data point, corresponding to the bottom 50–60% of the profile, were always used to fit the line core to the polynomial.

Series of measurements of this kind cannot by themselves tell whether changing line minima are due to the entire line shifting, as in the Doppler effect, or variations in the line shape; thus the measurements are affected by both of these possible causes.

2.2. Physical Interpretation of the Measured Velocities

While fitting a polynomial to the line core is a common means of measuring wavelengths (Sabbey *et al.* 1995 for example), it is not intuitive what such a measurement physically means in a star whose absorption lines are known to be slightly asymmetric (Leckrone 1971) due to the effects of nonradial pulsations. For a symmetric absorption line, it is obvious that the minimum of the line profile coincides exactly with the centroid of the line. The purpose of this section is to investigate how close this equality is for the slightly asymmetric lines that can occur in this star.

The blue observation, Image No. 940731.009, was chosen for this test because the S II absorption lines in it are slightly asymmetric. This is noticeable by inspection only when the line profiles are compared to those from observations that were taken immediately before and after 940731.009. In this spectrum, the line asymmetry parameter (as described in Section 3) of the S II $\lambda 5454$ has a value very close to that averaged over all 58 observations. Thus, the line asymmetry in the 940731.009 spectrum is representative of the overall level of line asymmetry in the observations. Table 7 compares the wavelengths of all the S II lines in this spectrum, as measured by the profile minima and the line centroids (as measured by the e–key in IRAF's SPLOT routine). Refer to Section 1 for the line identifications listed in the table.

Based on the last column of Table 7, the average difference and its standard deviation about this mean are +0.006 Å and 0.006 Å. For reference, 0.006 Å at a wavelength of 5454 Å corresponds to 0.3 km s^{-1} in radial velocity; this value is smaller than the estimate for the observational error in radial velocity that is found in Section 2.3 below. Thus, within a 1 sigma error bar, the difference between the two sets of measurements is statistically negligible.

Table 7: A Comparison of Wavelength Measurements

	Wavelength (Å)		
Blue Line No.	(Profile Minimum)	(Centroid)	Difference (Å)
3	4152.881	4152.898	0.017
4	4162.487	4162.495	0.008
6	4394.217	4294.224	0.007
20	5103.124	5103.130	0.006
21	5200.785	5200.785	–0.000
22	5212.417	5212.419	0.002
23	5320.483	5320.494	0.011
24	5345.474	5345.484	0.010
25	5453.611	5453.607	–0.004
26	5473.371	5473.375	0.004

The radial velocities in this work, while calculated from the line minima, are statistically equivalent to velocities based on line centroids because the line asymmetry of S II (6) $\lambda 5454$ is quite small in the current observations. Therefore, these results are directly comparable to sets of radial velocities that are based on line centroid wavelengths.

2.3. Estimation of the Observational Error

In order to determine the observational error associated with the radial velocity measurements, 25 observations of 6 G and K–type giant stars that are radial velocity standards were obtained on some of the nights on which ι Her was observed. For each standard, Table 8 shows the published values of the radial velocity taken from The Astronomical Almanac (1992) and the number of observations.

Table 8: Radial Velocity Standards

Standard	Published Velocity (km s^{-1})	# of Observations
α Boo	-5.3 ± 0.1	15
β Oph	-12.0 ± 0.1	2
α Cas	-3.9 ± 0.1	4
α Tau	54.1 ± 0.1	1
ϵ Peg	5.2 ± 0.2	1
ϵ Leo	4.8 ± 0.1	2

To verify that these stars are stable radial velocity standards, a detailed literature search was conducted in the SIMBAD astronomical database. Of the 6 standards, only α Cas and ϵ Peg had no reported evidence of velocity variations in the database. In all of the remaining stars, the intrinsic velocity variations were extremely small with the exception of α Boo. Because α Boo was (by far) the most commonly observed standard star in this work, had the largest reported velocity variation of the standards, and was the only standard whose velocity variation was detected by 2 or more independent groups, it is important to consider it in detail.

Table 9: Reported RV Variability in α Boo

Period (days)	Amplitude (m s^{-1})	Reference(s)
2	200	Smith, McMillan & Merline 1987 Cochran 1988 Innis *et al.* 1988
2.46	54	Hatzes & Cochran 1994
4.03	30	Hatzes & Cochran 1994
8.52	14	Hatzes & Cochran 1994
11.6	60	Belmonte *et al.* 1990
223	500	Hatzes & Cochran 1993

The variability that is described in Table 9 has periodicities and amplitudes that may (if they are real) affect our observations of α Boo. Because the derived observational error depends heavily upon the observations of α Boo, it is a conservative upper limit for the true observational error.

The errors were estimated from measuring 5 Fe I lines in each of the radial velocity standards using the method described above in Section 2.1 The wavelengths of these lines (Moore 1959) are $\lambda\lambda$5445.045, 5455.613, 5461.540, 5466.404, and 5466.993. Since they occur in the small region where the blue and red observations overlap, the wavelength errors that arise from the wavelength–calibration part of the reduction will affect the Fe I lines in the same manner that they affect the S II (6) λ5454 line. This error estimate therefore applies to both the blue and red observations.

Inspection of the 5 Fe I lines in a spectrum of α Boo (Image No. 940513.014) reveals that they are relatively weak lines in the giant spectra with an average FWHM of about 0.27A and an average residual intensity of 0.6 in normalized flux. The S II line in ι Her has an almost identical FWHM (0.28Å in image No. 940609.016) and a typical residual intensity of 0.8 in normalized flux. Thus, the Fe I lines in the giant spectra are similar in strength and shape to the S II line in the ι Her spectra and, therefore, should yield a similar uncertainty in the measurement of radial velocities.

Table 10 lists the mean heliocentric radial velocity based on the 5 Fe I lines (called V in the table) and the standard deviation of the 5 values about the mean (called σ in the table) for each spectrum of the radial velocity standards. Three observations yielded heliocentric radial velocities that are drastically different from the published values; these observations are marked with * and were not used to compute errors.

The radial velocities in Table 10 can be used in two ways to compute the error in the radial velocity measurements. One method is to compute the rms deviation of the measured heliocentric radial velocities from the published values given in Table 8. The standard deviation calculated in this manner gives 0.5 km s^{-1} as the error. The second method, which is to compute the rms deviation of the measured heliocentric radial velocities from their mean, is described below. Table 11 gives the mean value and rms deviation of the radial velocities (V) from Table 10, calculated separately for each standard.

The standard deviations in Table 11 form an average (weighted by the number of observations of each standard) that gives the error based on the mean velocity of 5 lines; to compute the error based on the measurement of just 1 line, this weighted average is multiplied by the square root of 5. The error in the measurement of 1 line, calculated in this manner, is 0.7 km s^{-1}. Because of the intrinsic variations known

Table 10: Measurements of Radial Velocity Standards

Image No.	V (km s^{-1})	σ (km s^{-1})
	α Boo	
940628.001*	– 3.43	0.70
940731.007*	– 4.34	0.66
940513.014	– 5.31	0.46
940520.017	– 5.32	0.70
940521.017	– 5.43	0.56
940528.012	– 5.27	0.55
940529.004	– 5.50	0.47
940607.012	– 5.24	0.60
940609.014	– 5.51	0.45
940610.001	– 5.17	0.63
940611.012	– 4.77	0.56
940701.011	– 5.10	0.70
940711.022	– 5.52	0.45
950303.022	– 5.58	0.52
950311.004	– 5.93	0.56
	β Oph	
940630.012	–11.16	0.74
940904.018	–12.96	0.75
	α Cas	
940817.027	– 3.53	0.64
940908.021	– 3.43	0.48
940930.024	– 3.41	0.62
941111.030	– 4.25	0.68
	α Tau	
940206.010	54.05	0.90
	ϵ Peg	
940811.016*	2.97	0.40
	ϵ Leo	
950303.030	3.86	0.96
950304.033	3.99	0.99

to occur in α Boo, this figure should be considered as a conservative upper limit to the true observational error. Correcting for the best confirmed intrinsic variation in α Boo (period=2 days, amplitude=200 m s^{-1}) yields an error of 0.5 km s^{-1}. The intrinsic variations in α Boo are likely to be due to radial pulsations and some researchers have suggested that α Boo is changing radial pulsation modes on time scales of a few years (Hatzes & Cochran 1994).

The two methods described above agree with each if one takes into account the intrinsic velocity variations that have been observed in α Boo. Because of the

Table 11: Determination of Radial Velocity Observational Error

Standard	Number	Mean (V) in km s^{-1}	σ(V) in km s^{-1}
α Boo	13	– 5.36	0.27
β Oph	2	–12.06	...
α Cas	4	– 3.65	0.35
α Tau	1	54.05	...
ϵ Leo	2	3.92	...

uncertainties introduced by the intrinsic velocity variability in α Boo, 0.7 km s^{-1} will be taken as the estimate for the observational error in the radial velocity measurements (conservative though it may be).

2.4. S II (6) λ5454 HRV

This section presents the heliocentric radial velocities of the S II λ5454 line based on the observed wavelengths as measured with the method described in Section 2 Figure 2 shows the HRV curve; notice the clear variation that is due to the orbital motion of ι Her. In the remainder of this work, any references to velocity or radial velocity refer to heliocentric radial velocity.

Table 12: The S II (6) λ5454 HRV

HJD (2449000.+)	HRV (km s^{-1})	HJD (2449000.+)	HRV (km s^{-1})
389.9589	-18.5	574.7255	-22.0
444.8891	-20.9	581.5824	-21.3
485.7911	-23.1	581.6024	-22.0
490.7673	-24.3	581.6204	-21.8
490.7784	-25.3	581.6386	-22.1
491.7902	-21.7	581.6579	-22.2
492.7008	-18.2	581.6947	-21.9
493.7967	-22.7	594.7509	-30.1
495.7611	-17.3	594.7644	-30.8
500.7418	-16.8	599.5956	-26.7
501.7119	-18.7	599.6268	-27.3
501.7201	-18.3	599.6804	-26.2
501.7293	-19.6	603.5936	-21.4
506.7050	-17.0	603.6183	-21.4
510.7306	-15.7	603.6427	-21.3
510.7469	-15.8	603.6907	-21.1
512.6654	-13.5	613.5981	-18.4
513.7287	-16.9	625.5192	-15.8
514.6642	-15.8	625.5432	-15.3
531.6722	-12.7	625.5670	-15.6
533.6473	-16.2	625.5906	-15.9
534.6291	-13.0	625.6147	-15.6
544.6914	-17.2	625.6405	-16.3
564.5899	-18.7	653.5462	-15.0
564.6800	-19.8	653.5690	-15.5
564.7043	-20.1	667.5150	-17.4
564.7286	-19.9	778.9597	-20.2
564.7530	-20.9	779.8612	-18.8
564.7711	-20.7	786.9398	-19.1

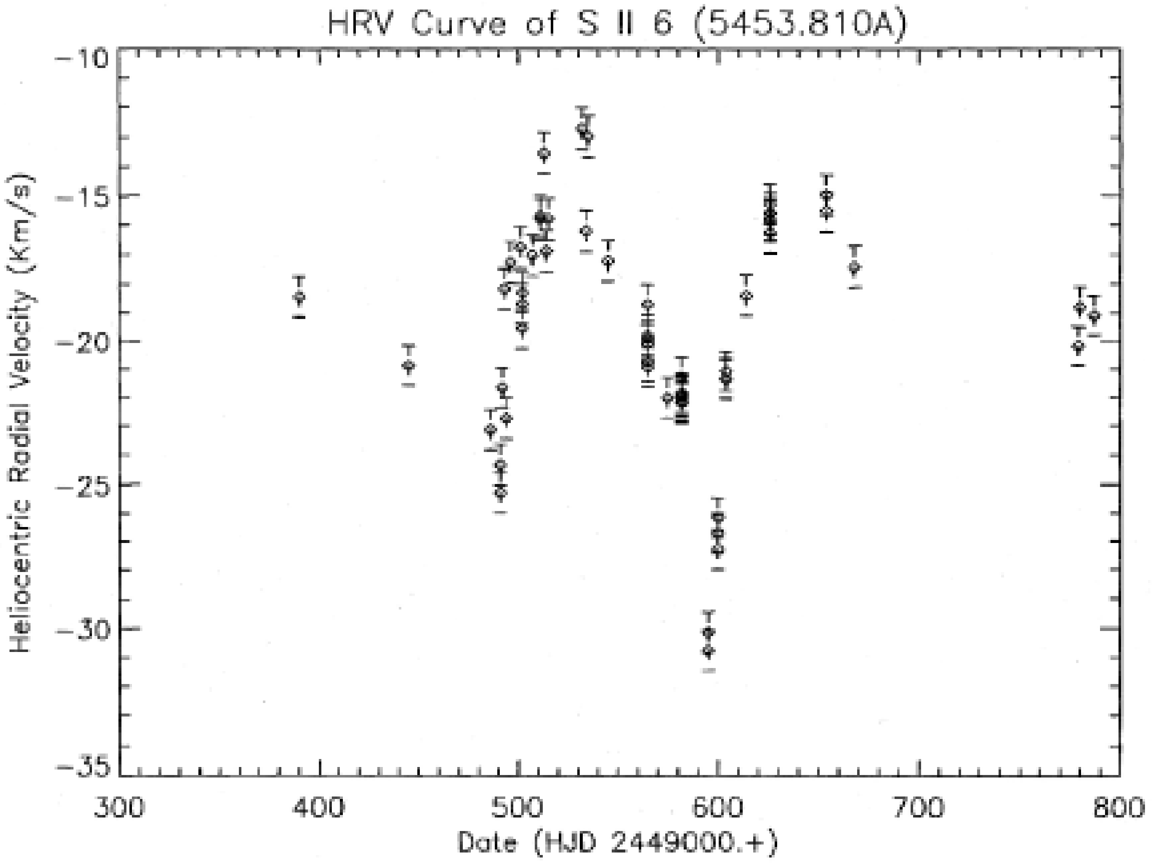

Fig. 2.— The HRV of S II (6) λ5454.

2.5. The HRV of Other Absorption Lines

In order to test whether or not the radial velocity variations in S II λ5453.810 are representative of the variations that the star undergoes, the radial velocities of this S II line were compared to the velocities based on 8 other absorption lines of similar strength, measured by the same method. The error in the velocity measurements of these 8 lines is assumed to be the same as that estimated for S II λ5454 in Section 2.3 For each of these 8 lines, the measured radial velocities were subtracted from the S II λ5454 radial velocities. The mean (ΔV) and standard deviation about the mean (σ) of this difference, and the linear correlation coefficient (R) were calculated. Table 13 gives the results.

Table 13: Comparison of the S II HRV to that of Other Lines

Line	Identification	ΔV(km s^{-1})	σ(km s^{-1})	R
Si III λ4568	blue 14	1.5	0.7	0.969
S II λ5474	blue 26	1.0	0.5	0.982
S II λ5429	red 1	1.1	1.5	0.972
S II λ5433	red 2	0.6	1.8	0.962
S II λ5565	red 4	0.7	1.3	0.980
S II λ6347	red 9	1.0	0.7	0.994
Ne I λ6402	red 12	1.2	0.8	0.993
C II λ6578	red 14	0.5	0.7	0.994

The results from Table 13 show that the radial velocities based on S II λ5454 are consistently larger than those based on other lines by an average of 1.0 km s^{-1}. This shift may indicate that S II λ5454 is blended or that the rest wavelength given by Moore is incorrect (or both). The line asymmetry data given in Section 3.3 show that the average value of the line asymmetry is essentially zero (1×10^{-5}Å); this indicates that the systematic difference is due not to blending but to an incorrect rest wavelength. Then, the rest wavelength of the S II line is too large by approximately 0.018Å and the correct rest wavelength is 5453.792Å. An important implication of this result is that the orbital element γ, the radial velocity of the center of the binary's mass, will be too large by an amount of 1.0 km s^{-1}. Because any errors in the assumed rest wavelength of the S II line will be absorbed into the derived value of γ. The residual velocities will be unaffected by use of the incorrect rest wavelength.

Five of the eight lines listed in Table 13 display a standard deviation that is virtually all accounted for by the observational error of 0.7 km s^{-1} (refer to Section 3.3); these lines are Si III λ4568, S II λ5475, S II λ6347, Ne I λ6402, and C II λ6578. This and the fact that the correlation coefficients are near 1.0 for all of the lines implies that these lines participate in the same velocity variations that the S II line exhibits. Thus, the velocity variations detected in the S II line are representative of those based on Si III, Ne I, C II, and other S II lines; the Si III comparison line has been used as an indicator of pulsation prior to this work (Smith 1978). The remaining three comparison lines show a large scatter; these three S II lines are among the weakest of the eight velocity comparison lines and therefore may be more affected by noise in the continuum.

Table 14: The HRV of Other Lines in the Blue Region

	HRV (km s^{-1})	
HJD	Si III λ4568	S II λ5474
531.6722	–17.4	–12.2
533.6473	–21.5	–17.1
564.5899	–23.0	–20.0
564.6800	–24.3	–20.9
564.7043	–24.9	–21.1
564.7286	–25.3	–20.6
564.7530	–25.9	–21.0
564.7711	–24.7	–22.4
581.5824	–25.0	–23.7
581.6024	–28.2	–22.9
581.6204	–25.9	–23.3
581.6386	–25.9	–22.7
581.6579	–26.8	–23.2
581.6947	–28.0	–22.9
603.5936	–24.4	–22.5
603.6183	–26.2	–22.8
603.6427	–25.6	–22.9
603.6907	–26.7	–22.5
625.5192	–20.1	–16.8
625.5432	–20.7	–16.1
625.5670	–20.0	–16.9
625.5906	–21.0	–16.3
625.6147	–20.7	–16.9
625.6405	–20.1	–16.9
653.5462	–19.5	–16.2
653.5690	–20.3	–16.8

Table 15: The HRV of Other Lines in the Red Region

	HRV (km s^{-1})					
	S II	S II	S II	S II	Ne I	C II
HJD	λ5429	λ5433	λ5565	λ6347	λ6402	λ6578
389.9589	–19.81	–19.56	–17.94	–18.45	–18.98	–19.33
444.8891	–20.14	–20.30	–20.49	–20.90	–21.09	–20.33
485.7911	–25.03	–24.74	–24.88	–25.86	–25.66	–24.76
490.7673	–24.71	–25.64	–24.30	–25.28	–25.57	–25.28
490.7784	–24.44	–25.36	–23.71	–26.38	–26.09	–25.25
491.7902	–22.53	–21.42	–22.45	–22.92	–22.89	–22.10
492.7008	–18.55	–18.57	–18.12	–19.28	–19.08	–18.99
493.7967	–23.31	–22.36	–21.50	–22.98	–23.85	–22.98
495.7611	–18.66	–17.37	–18.17	–18.48	–18.35	–17.29
500.7418	–17.46	–17.72	–17.23	–18.67	–18.78	–19.12
501.7119	–18.96	–19.29	–17.82	–19.67	–19.00	–18.66
501.7201	–18.04	–18.04	–22.10	–19.84	–19.54	–18.75
501.7293	–22.98	–18.95	–20.49	–18.75	–18.36	–18.93
506.7050	–18.27	–17.35	–20.12	–17.71	–17.85	–17.38
510.7306	–17.51	–15.41	–19.22	–16.73	–17.54	–16.22
510.7469	–24.04	–16.29	–14.96	–16.94	–17.22	–16.35
512.6654	–14.68	–14.33	–13.89	–14.78	–15.30	–14.32
513.7287	–16.67	–16.82	–17.81	–18.88	–18.14	–17.59
514.6642	–17.12	–16.61	–15.55	–17.30	–17.37	–16.53
534.6291	–13.42	–13.38	–13.63	–13.49	–14.24	–13.77
544.6914	–18.54	–15.27	–17.16	–17.10	–18.07	–16.83
574.7255	–22.61	–22.27	–22.94	–22.31	–23.13	–22.80
594.7509	–30.73	–31.59	–30.79	–31.92	–32.82	–30.90
594.7644	–30.81	–31.09	–30.51	–31.92	–32.57	–31.35
599.5956	–27.37	–36.67	–28.05	–27.73	–28.29	–27.04
599.6268	–27.39	–27.48	–28.62	–27.22	–27.50	–26.68
599.6804	–28.15	–26.62	–27.67	–27.34	–27.44	–26.48
613.5981	–20.00	–19.77	–18.99	–19.98	–20.91	–20.05
667.5150	–17.94	–17.48	–18.89	–17.75	–18.99	–17.42
778.9597	–20.76	–20.84	–20.47	–20.52	–20.38	–20.14
779.8612	–20.49	–19.86	–22.04	–19.99	–20.42	–20.40
786.9398	–20.09	–19.50	–19.83	–21.07	–20.75	–20.75

3. Equivalent Width & Line Asymmetry Measurements

The equivalent width (W_λ) and line asymmetry of S II λ5454 were measured in order to describe the nature of periodic variations in the radial velocity of the S II line; for example, are the observed velocity variations accompanied by detectable changes in equivalent width?

Equivalent width (W_λ). The equivalent width of an absorption line is defined to be the width of a column that extends from the zero flux level to the local continuum such that the area in the column is equal to the area between the local continuum and the line profile divided by the flux of the local continuum. When the flux scale is normalized such that the local continuum flux is set to a value of 1.0, the equivalent width is equal to the area between the local continuum and the line profile and therefore is a measure of the line strength.

Line asymmetry. The line asymmetry parameter used in this work (hereafter simply called the "line asymmetry") is defined in the following manner:

$$\text{Line Asymmetry} = W_\lambda(\text{lhs}) - W_\lambda(\text{rhs})$$

where the W_λ(lhs) is the contribution to the total equivalent width from the portion of the line profile to the left hand side of the wavelength of minimum flux and W_λ(rhs) is the contribution from the portion of the line profile that is to the right hand side. This approach has been used in the study of line profile variations in classical Cepheids (Sabbey *et al.* 1995).

3.1. Description of the Method

The W_λ's and line asymmetries were calculated in the following manner. The spectra of ι Her were continuum normalized by a 3rd degree spline fit using the standard

IRAF routine CONTINUUM, and the wavelength of minimum flux was determined in the manner described in Section 2.1 Then, the values of W_λ(lhs) and W_λ(rhs) were determined from a numerical integration using a trapezoidal rule from the wavelength of minimum flux to the left and right hand terminus of the absorption line profile. The left hand terminus of the line, for example, was determined in the following interactive manner.

The plot of enclosed equivalent width versus wavelength was displayed on a computer screen, where the 'enclosed equivalent width' refers to the area contained within the line profile as integrated from the wavelength of minimum flux to a particular wavelength. The left hand portion of the line profile was then overplotted on the computer screen.

As one starts at the wavelength of minimum flux and integrates toward the left side of the line profile, the enclosed area (i.e. enclosed W_λ) increases. But when the integration is carried past the left hand terminus of the line profile and into the surrounding noise, the enclosed area no longer increases or decreases due to cancellation of the positive and negative noise peaks. Thus, by locating where the enclosed area flattens out, one is locating the terminus of the line profile; the value of W_λ(lhs) is then the value of the enclosed area at the point where is flattens out.

By simultaneous inspection of the left hand side of the line profile and the value of the enclosed area at points along the profile, a very accurate determination was made of the left hand terminus of the line profile and, therefore, W_λ(lhs). This method largely removed one of most problematic uncertainties that are inherent in equivalent width measurements: the placement of the integration limits.

The measurement was repeated for the right hand portion on the S II line; resulting in the measurement of W_λ(rhs). The W_λ and line asymmetry were then determined.

3.2. Estimation of the Observational Error

The measurements described in this section depend upon the accurate placement of the local continuum around the S II λ5454 line and also on the photon or shot noise. In the literature, a canonical value for the error (around 10%) is usually assigned to equivalent widths and other measurements that depend upon the continuum placement. The region around the S II line is free of features that may contribute to errors in the continuum placement (eg. broad lines/wings of Balmer lines and He I, telluric absorption lines from water, interstellar lines, nearby strong absorption lines, etc...). For this reason and because of the high quality of the observations (average SNR around 100), this author suspected that the canonical value of ± 10% may overstate the errors caused by continuum placement.

In order to calculate the uncertainty in these measurements due to the placement of the continuum, the following method was employed. For 5 randomly selected observations in the blue and 5 randomly selected observations in the red, the full width (W) of the S II line at the continuum was measured in the normalized spectra (F_c was assumed to be 1). The continuum was then raised and lowered in these observations until (by inspection) it was obvious that the continuum was too high and too low. The amount that the continuum was raised and lowered was recorded as E+ and E–; the average uncertainty in the continuum placement is then given as E = 0.5(E+ + E–). The iraf routine CONTINUUM only considers fluxes within 2 standard deviations of their local continuu in the normalization; with the average SNR = 100, the maximum value of E should be around 0.02 units of normalized flux. The values of E that were obtained from inspection are all below the expected upper limit.

The values W, F_c, E, and the equivalent widths (W_λ) were used to estimate the uncertainty in the W_λ measurements. The following formula (derived in Appendix

B) was used to estimate the uncertainty in the measurements due to uncertainty in the placement of the continuum.

$$\mathrm{d}(W_\lambda) = (\ \mathrm{E}\ /\ F_c\ )\ [\ \mathrm{W} - W_\lambda\ ]$$

For the 5 observations in each region, the individual uncertainties were used to compute the average uncertainty. The final estimate for the uncertainty in the W_λ was calculated as the mean (weighted by the total number of observations in each region) of the average uncertainty determined for each region. The uncertainty, calculated in the this manner, was found to be 0.006Å. This value is taken as the uncertainty in all W_λ measurements caused by continuum placement; notice that this value is very close to the canonical value of 10%. To first order, and under the assumption of symmetric integration limits, the uncertainty in the continuun placement does not affect the line asymmetry measurements.

Table 16: Uncertainty in W_λ

HJD	W(Å)	E+	E–	W_λ(Å)	d(W_λ) (Å)
Blue					
531.6722	0.745	0.027	0.006	0.055	0.011
533.6473	0.622	0.015	0.007	0.059	0.006
564.5899	0.646	0.014	0.002	0.060	0.005
581.6024	0.849	0.009	0.004	0.059	0.005
603.6907	0.602	0.007	0.013	0.064	0.005
Red					
490.7673	0.469	0.009	0.009	0.060	0.004
491.7902	0.574	0.009	0.011	0.060	0.005
510.7306	0.603	0.014	0.007	0.060	0.006
667.5150	0.532	0.012	0.013	0.062	0.006
778.9597	0.590	0.010	0.010	0.060	0.005

IN addition to the continuum placement, photon noise may contribute to errors in the W_λ measurements and is the dominant cause of error in line asymmetry measurements. The effect of photon noise depends critically upon the shape and strength of the absorption line being measured and the number of data points that make up the line. In order to test this effect, 1000 synthetic line profiles of the S II line were created with photon noise added. The lines were modeled by a gaussian shape with a W_λ and residual intensity (RI) equal to 0.62Å and 0.2 units of normalized flux, similar to the average values for S II λ5454. The signal–to–noise ratio at the continuum (SNR_c) was assumed to be 100. The magnitude of the photon noise as a function of normalized flux (F) was determined by the following model: magnitude of the noise = $\sqrt{(F)}\ /\ SNR_c$ and the noise spikes had equal likelihoods of being positive, negative, and zero. The line profiles were sampled by 11 points (just enough to include the line) at the dispersion of 0.05 Å per data point (which closely approximates the dispersion of the spectra around the S II line). The W_λ of the 1000 synthetic lines were measured giving a standard deviation about the mean (an estimate for the observational error due to photon noise) of 0.001Å.

The total uncertainty in the W_λ is the sum, in quadrature, of the uncertainties due to continuum placement and photon noise while photon noise represents the uncertainty in the line asymmetry measurements. The total uncertainty in W_λ is dominated by the uncertainty due to continuum placement and is equal to 6mA; this value will be taken as the observational error in the W_λ and line asymmetry measurements.

3.3. Measurements of S II (6) λ5454

The equivalent width and line asymmetry of the S II λ5454 line were measured with the method described in Section 3.1. Table 17 shows the results; recall that the observational error associated with the W_λ measurements is 0.006Åand that associated with the line asymmetries is 0.001Å.

Table 17: W_λ and Line Asymmetry Measurements of S II λ5454

HJD	W_λ(Å)	Line Asymmetry (Å)	HJD	W_λ(Å)	Line Asymmetry (Å)
389.9589	0.068	–0.001	574.7255	0.058	0.000
444.8891	0.085	0.003	581.5824	0.061	0.007
485.7911	0.061	0.001	581.6024	0.059	0.001
490.7673	0.060	–0.002	581.6204	0.057	0.003
490.7784	0.061	0.002	581.6386	0.057	0.002
491.7902	0.060	–0.002	581.6579	0.059	0.003
492.7008	0.064	0.002	581.6947	0.054	0.002
493.7967	0.062	–0.003	594.7509	0.058	0.000
495.7611	0.059	–0.003	594.7644	0.056	0.003
500.7418	0.059	0.003	599.5956	0.058	–0.002
501.7119	0.063	–0.002	599.6268	0.060	–0.003
501.7201	0.063	–0.002	599.6804	0.062	0.000
501.7293	0.061	–0.009	603.5936	0.058	0.000
506.7050	0.063	–0.002	603.6183	0.060	–0.002
510.7306	0.060	0.002	603.6427	0.059	–0.001
510.7469	0.064	0.000	603.6907	0.064	–0.002
512.6654	0.065	–0.002	613.5981	0.057	0.000
513.7287	0.059	0.003	625.5192	0.060	–0.004
514.6642	0.060	0.003	625.5432	0.061	0.000
531.6722	0.055	0.003	625.5670	0.062	–0.002
533.6473	0.059	0.001	625.5906	0.061	–0.002
534.6291	0.061	–0.003	625.6147	0.056	0.001
544.6914	0.059	–0.006	625.6405	0.058	–0.005
564.5899	0.060	0.002	653.5462	0.059	0.001
564.6800	0.061	0.001	653.5691	0.060	–0.002
564.7043	0.059	0.000	667.5150	0.062	0.000
564.7286	0.062	–0.002	778.9597	0.060	–0.003
564.7530	0.061	–0.001	779.8612	0.062	0.004
564.7711	0.059	–0.003	786.9398	0.063	0.001

The W_λ values show variations from 0.056 Å to 0.064 Å; thus the range of variations seen (0.008 Å) is only slightly larger than the uncertainty in the measurements (0.006 Å). Because of this, caution should be used in interpreting variations seen in the W_λ measurements. The line asymmetry is very small, indicating that the S II λ5454 line is fairly symmetric. Because of the small values of the line asymmetry parameter, it will not be used to study pulsations that occur in ι Her.

Chapter 4

Data Analysis

1. Determination of the Orbit

Iota Her is the primary star in a single–lined spectroscopic binary. The orbital elements have been derived by previous investigators (Abt & Levy 1978). Kodaira (1971) estimated the orbital period, γ, and K. In order to study pulsation in ι Her through their effect on the observed HRV of absorption lines, one must subtract out the radial velocity variations that are caused by the star's motion in its binary orbit. Previous determinations of the binary orbit have, however, been somewhat less than definitive for the following reasons.

(1) The previous determinations of the orbit used data that did not completely cover all phases of the orbit; these data are usually sparse and are taken from many different epochs of the orbit. For example, Abt & Levy (1978) attempted to use 20 spectra taken over 5 orbital cycles in their determination. They had to combine their data with previously published data (Petrie & Petrie 1939) in order to have complete phase coverage of the orbit.

(2) The radial velocity measurements upon which the previous orbit determinations were less precise than the present data set. For example, the standard error (s.e.) in the radial velocity measurements used by Abt & Levy (1978) ranges from a standard error (s.e.) from 0.9 km s^{-1} to 2.2 km s^{-1} while the mean standard error in the radial velocity measurements used by Kodaira (1971) is 1.0 km s^{-1}. The observational error of the present radial velocity data is only 0.7 km s^{-1} (Chapter 3, Section 2.3).

(3) The previous orbit determinations do not take into account the fact that pulsations in a star like ι Her can contribute to radial velocity variations. Because the times cale of pulsations in B stars is short compared to a typical orbital period, it is often assumed that the pulsational contributions to radial velocity variations will average out in such a way that they do not affect the orbit determination. In the case of ι Her, however, these assumptions are not valid for two reasons: the amplitude of radial velocity variations due to pulsation is comparable to that which is due to the binary orbit; and the fact that ι Her is known to be multiperiodic with non–radial pulsation modes makes it possible that the radial velocity variations of two modes with similar periods can produce a beat velocity variation whose period is a significant fraction of the orbital period.

Calculation of the Binary Orbit

The binary orbit was calculated using an iterative process that takes into account the dominant residual velocity variation as well as the velocity variation due to the orbital motion of ι Her about the center of mass of the binary system; the term "residual" will be used often in this thesis and will refer to the data set after the orbital velocity variations have been subtracted out (i.e. prewhitened for the orbit). Below are basic definitions of quantities that describe the orbit of a single–lined spectroscopic binary with respect to the center of mass:

P = The orbital period.

γ = The radial velocity of the center of mass of the binary system.

K = The half–amplitude of the radial velocity variations caused by the motion of the primary in its binary orbit.

e = The eccentricity of the orbit.

Ω = The longitude of the periastron.

T_o = The time of periastron passage, any date when the primary is at periastron.

Periastron = The time when the primary is closest to the center of mass (and to the secondary as well).

i = The inclination of the binary orbital plane with respect to the plane of the sky; i = 90^o means that the line of sight (l) coincides with the plane of the orbit.

$a_1$sin$i$ = The projection of the semi–major axis of the primary's orbital motion on the line of sight.

f(m) = The mass function, which depends on i, the mass of the primary (m_1), and the mass of the secondary (m_2).

The following method that was used to calculate the binary orbit.

Step 1) Calculate the least–squares orbital solution based on the unaltered radial velocities of the S II line. This orbital solution is called the iteration 0 solution.

Step 2) Prewhiten the data for the radial velocity variations predicted by the orbital solution from Step 1. Determine the period of the dominant velocity variation in the residual using a Lomb periodogram (refer to Appendix A). The spacing in all Lomb periodograms used in this work is 0.024d, giving an uncertainty in any one period of ± 0.012d.

Step 3) Begin an iterative process as described below.

Step 3.1) Fit a least-squares Fourier–harmonic series to the dominant period in the residuals. The first time that this is done, the fit is called the iteration 0 fit.

In all 'Fourier–harmonic' fits described in this work, the series is fitted to a function of the variable (X) where X = MOD[2π (HDJ-HDJ_o)/Period] - 0.5; the value of HDJ_o is arbitrary and was taken as the HJD of the earliest observation (HJD 389.9589) unless otherwise noted. The form of the fitted function is as follows:

$$\text{Fit} = 0.5\ A_0 + A_1\cos(\text{X}) + B_1\sin(\text{X}) + ... + A_n\cos(\text{nX}) + B_n\sin(\text{nX})$$

The series was carried out to the number of terms (n) that minimized the variance in the residuals about the series. The harmonic terms were included to take into account the fact that pulsations in some stars (e.g. classical Cepheids) are observed to have a form that includes harmonics (i.e. they are not sinusoidal); the residual radial velocities in ι Her will also prove to be non–sinusoidal.

Step 3.2) Subtract the fit obtained in Step 3.1 from the radial velocities of the S II line.

Step 3.3) Calculate a new least–squares orbital solution on the data set obtained in Step 3.2.

Step 3.4) Prewhiten the radial velocities of the S II line by the new orbital estimate obtained in Step 3.3.

Step 3.5) Repeat the process (i.e. go back to Step 3.1) until the variance in the radial velocities of the S II line (prewhitened by the orbital solution and then prewhitened by the fit to the dominant residual period) is minimized.

The preceding iterative method works in the following manner. The form of the dominant residual variation is approximated by a Fourier–harmonic series. When this is subtracted from the S II radial velocities, the orbital radial velocity variations become less obscured by the residual variations. This allowed for a more precise determination of the binary orbit solution; subtracting this more precise orbit from the data made the residual variations less obscured allowing its form to be better determined. The process continues in this manner, each iteration simultaneously giving a more precise fit to the orbit and the residual variation. The least–squares solution is achieved when the orbit solution combined with the fit to the residual variation (here 3.86d) minimizes the variance (i.e. the least–squares solution is the one where the value of ∇_2 in Table 18 is a minimum).

The calculation of the least–squares binary orbital solutions that is described in Steps 1 and 3.3 was performed with the FORTRAN code described by Wolfe *et al.* (1967). The numerical method used by the code is a Wilsing–Russell method (modified to work for both high and low eccentricity orbits) followed by a differential correction. The code requires (besides a set of radial velocities) only an initial guess for the period; for the iteration 0 orbit solution, the period determined from Abt & Levy (1978) was used as the initial period and for other iterations, the period determined from the past iteration was used.

For each iteration of the above–described process, the following items were calculated: the orbital elements, the period of the dominant residual variation, the amplitude and phase associated with this period (taken from the fundamental term in the Fourier–harmonic series), the variance after the S II radial velocities were prewhitened for the orbital solution (called ∇_1 in Table 18), and the variance after the S II radial velocities were prewhitened for both the orbital solution and the fit to the dominant residual period (called ∇_2 in Table 18). Table 18 shows these values (with the standard errors omitted for the orbital elements). The amplitudes and phases in Table 18 and in the rest of this work come directly from the fundamental component of the Fourier-harmonic fit and are rendered in the following manner:

$$\text{Fundamental Fit} = \text{Amplitude} \times \cos(\text{X–Phase})$$

where X has been previously defined and the amplitude and phase are related to the

A_1 and B_1 coefficients from the Fourier–harmonic series by the following.

$$\text{Amplitude} = \sqrt{A_1^2 + B_1^2}$$
$$\text{Phase} = \arctan B_1/A_1$$

In order to illustrate how the iterative process works, it is followed through iteration 0. Figure 3 shows the orbit determined from the unaltered data (iteration 0), compared to the observed radial velocities of S II as a function of orbital phase instead of time. Figure 4 shows the observed radial velocities prewhitened by the radial velocity variations predicted by the initial orbit solution. Notice that the residuals show scatter well beyond that expected from the observational error of 0.7 km s^{-1} (as indicated by the error bars). Figure 5 shows the periodogram of the residuals from the initial orbit. The peak at 3.864d is the strongest peak in the periodogram indicating that a 3.864d variation is the strongest overall in the data. In all iterations of the orbit solution, the dominant residual variation had this period. Finally, Figure 6 shows the residuals from the initial orbit phased to a period of 3.864d. The Fourier–harmonic fit (using 3.86d as the fundamental) is overplotted. The fit that is displayed in Figure 6 was subtracted from the radial velocities to provide the data set upon which the iteration 1 orbit was determined.

Table 18 shows that the iterative technique of accounting for a residual velocity variation works extremely well, converging rapidly. The best solution is the one that minimizes the value of ∇_2, thus the iteration 3 solution best fits the data. The iterative process cut the variance of the data about the combined orbit+Fourier–harmonic fit almost in half with most of the reduction resulting from an improved fit to the 3.864d residual period. A welcome outcome of the iterative process was that the fit to the orbit was better in the final solution (iteration 3) than it was in iteration 0 (albeit by only 5% in terms of the reduction in variance); apparently the more accurate description and removal of the residual

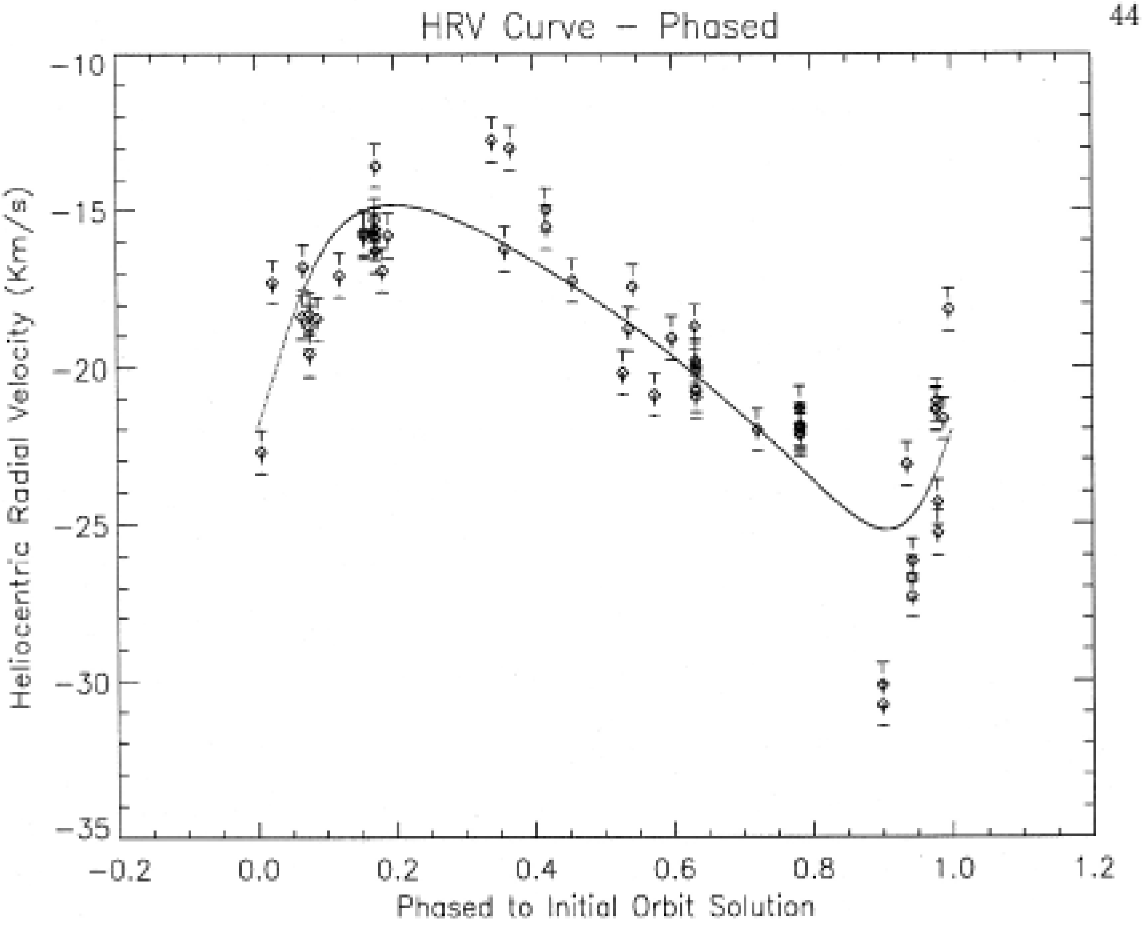

Fig. 3.— The initial orbit phased and compared to the observed S II HRV curve.

variation enabled the orbit determination program to find a better solution in the 6 dimensional parameter space. It is also evident that taking into account the dominant residual velocity variation did affect the orbit determination, particularly the derived period and the velocity semi–amplitude (K); refer to Figure 7 for a visual comparison of the final orbit to the initial orbit determination. In the remainder of this work, the final orbit is the iteration 3 solution.

The comparison of the S II radial velocities to other lines (Chapter 3, Section 2.5) suggests that γ is too large by a value of 1.0 km s^{-1}. If this is correct, then the final value of γ (–19.9 km s^{-1}) should be –20.9 km s^{-1}. Hereinafter, the final value of γ will be given as –19.9 (–20.9) km s^{-1} to indicate the possibility that γ calculated

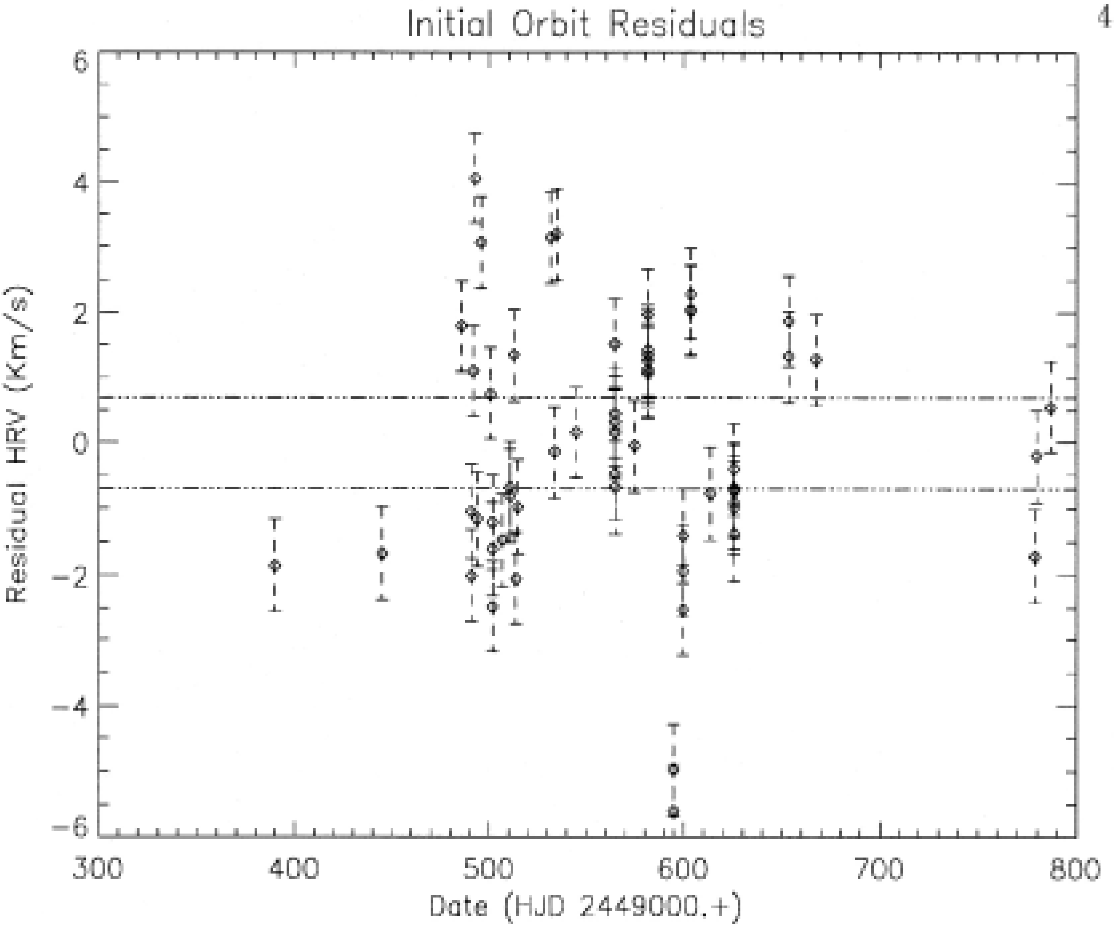

Fig. 4.— The residuals From the initial orbit.

from the S II HRV may be too large. The calculated value of γ (–19.9 km s^{-1}) will be the value used whenever the radial velocity data set is prewhitened for the final solution to the binary orbit.

Table 19 compares the final orbital elements to those calculated by Abt & Levy (1978) and Kodaira (1971). The standard errors (s.e.) (i.e. the 1 σ uncertainties) are also given. Figure 8 shows the radial velocity variations predicted by the final orbit in comparison to those predicted by the Abt & Levy (1978) orbit determination. There is general agreement between the final orbit computed for this work and the results of Abt & Levy (1978) and Kodaira (1971).

The final orbital elements can be used to determine properties of the binary

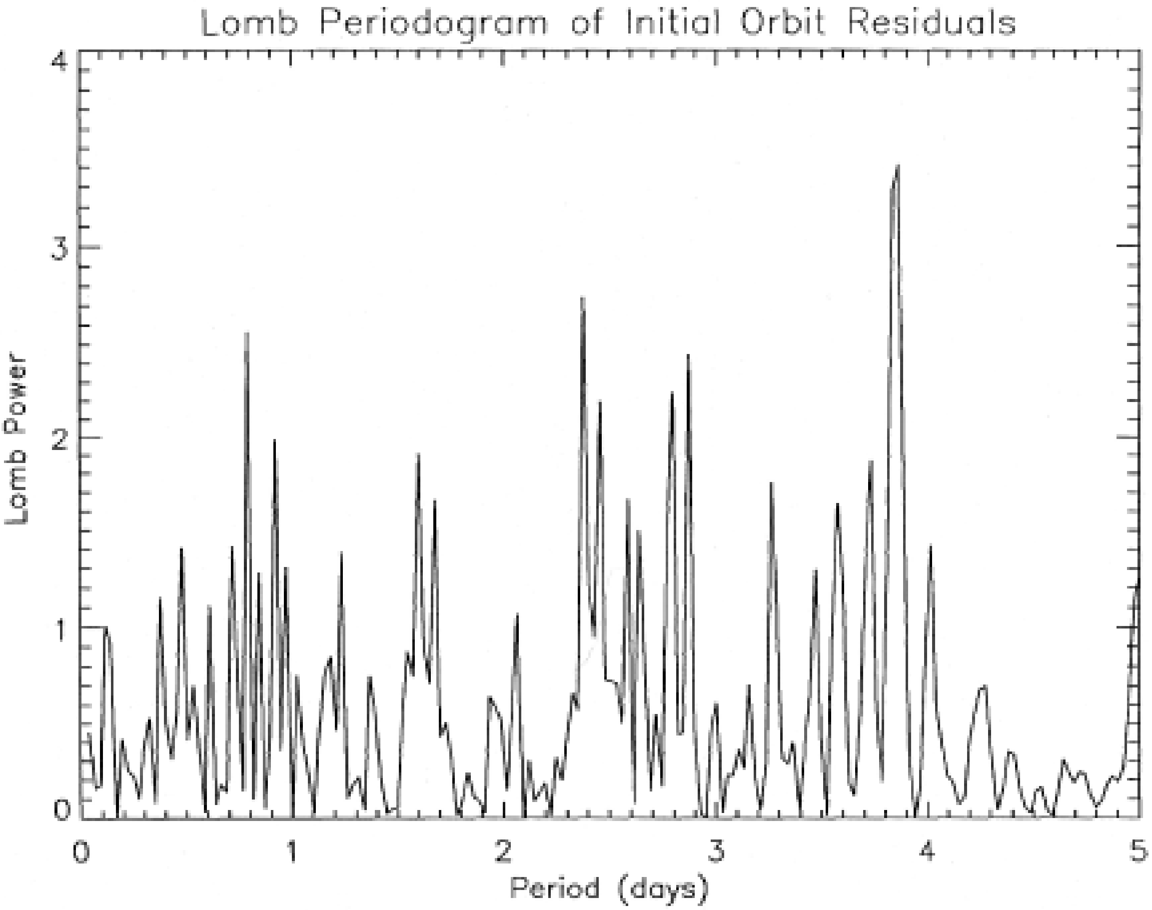

Fig. 5.— The periodogram of the residuals from the initial orbit.

system. The mass function, f(m), equals 0.0027 solar masses and the projection of iota Her's semi–major axis, $a_1$sin$i$, equals 14.31 solar radii. Under normal circumstances, no further information can be obtained about a single-lined spectroscopic binary like ι Her due to the unknown inclination angle. For ι Her however, the non-radial pulsations that it undergoes can yield information about its orbital inclination. Smith (1978), for example, found that line profile fitting suggested an inclination for the star's rotational axis of approximately 90°. Smith (1978) also takes that the mass of the primary star in ι Her to be around 8 solar masses, close to that of 7 solar mass star 53 Per (Stothers 1972), based on photometric and spectral–type similarity to the star 53 Per. Assuming that rotational and orbital angular momentum vectors

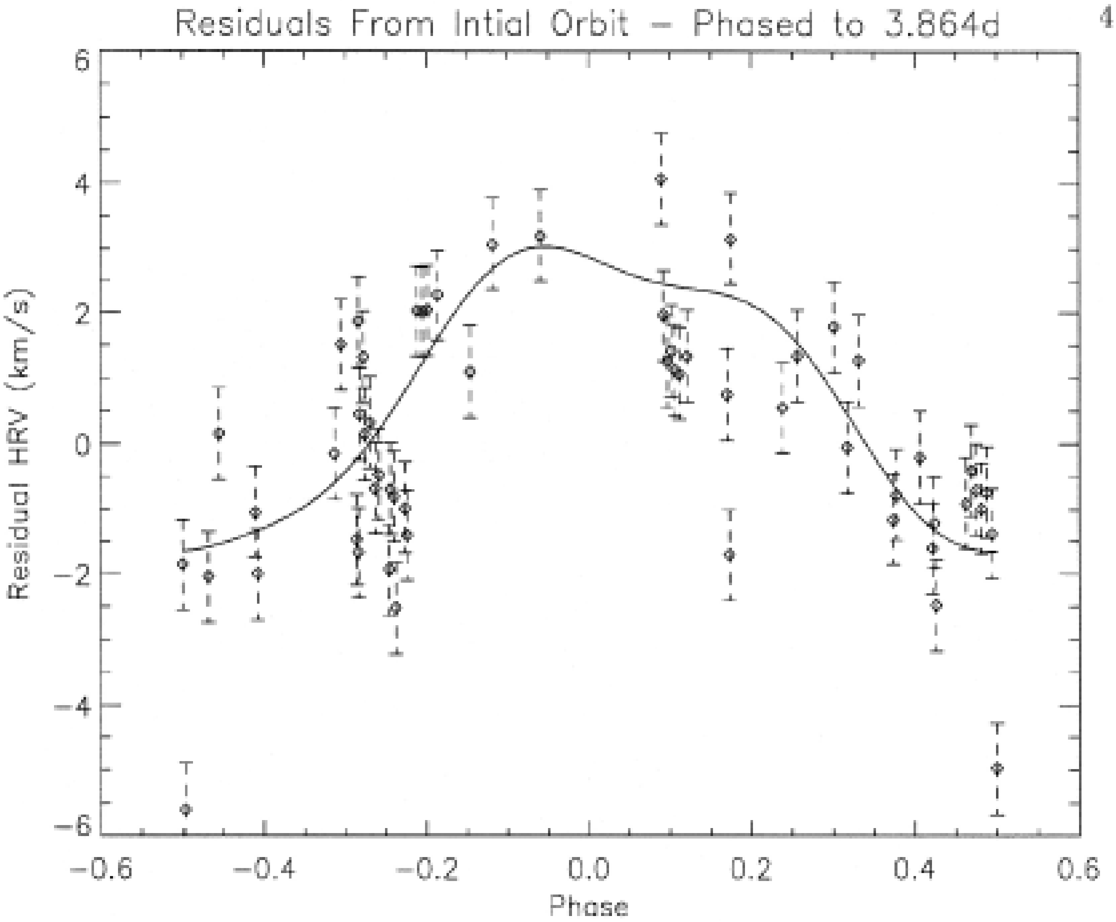

Fig. 6.— The initial orbit residuals phased to 3.864d and fitted to a Fourier–harmonic series.

are aligned and adopting the mass suggested by Smith (1978) yields a mass for the secondary (m_2) of 0.65 solar masses and a semi–major axis for ι Her (a_1) of 14.31 solar radii.

Mathias and Waelkens (1995) have recently questioned whether or not ι Her is actually a binary, suggesting that the periodic motion attributed to the binary orbit by Abt & Levy (1978) and Kodaira (1971) is actually due to beating among closely spaced non–radial pulsation modes. In this author's opinion, it is evident that ι Her is, indeed, a spectroscopic binary for at least two reasons. Orbit determinations have been made by three independent researchers (or groups): Kodaira in 1971, Abt &

Table 18: Orbital Solutions From Iterative Process

	Iteration Number				
Quantity	0	1	2	3	4
Period (days)	113.07	112.21	112.37	112.36	112.33
γ (km s^{-1})	–19.3	–19.6	–19.7	–19.9	–20.0
K (km s^{-1})	5.2	6.4	6.5	6.4	6.4
e	0.36	0.37	0.38	0.38	0.38
Ω (°)	248	226	219	218	218
To (HJD 2449000.0+)	267	264	262	262	262
∇_1 (km $s^{-1})^2$	3.45	3.23	3.18	3.28	3.40
Period (d)	3.864	3.864	3.864	3.864	3.864
Amp (km s^{-1})	2.4	2.2	2.1	2.1	2.1
Phase (rad)	0.154	0.249	0.246	0.257	0.259
∇_2 (km $s^{-1})^2$	2.02	1.24	1.19	1.18	1.19

Table 19: A Comparison of Orbit Determinations

	Final Orbit	Abt & Levy(1978)	Kodaira(1971)
Period (days)	112.36	113.804	112.7175
s.e.	0.79	0.016	...
γ (km s^{-1})	–19.9 (–20.9)	–20.0	–19
s.e.	0.2	0.2	...
K (km s^{-1})	6.4	5.4	6
s.e.	0.3	0.3	...
e	0.38	0.43	...
s.e.	0.04	0.04	...
Ω (°)	218	201	...
s.e.	6	8	...
T_o (HJD 2449000.0+)	262	203.5	...
s.e.	2	1.7	...

Levy in 1978, and this work in 1995. In all three of these cases, the derived orbit parameters are very similar and often agree with one another within mutual errors (refer to Table 19 and Figure 8). In the present work, the long term radial velocity variation (the 112.36d variation that is attributed to the binary orbit) was observed to exist through the entire data set that spans well over a year; refer to Figure 2. It is difficult to understand how the 112.36d variation could have remained so stable if it were due to a beating between two pulsation modes in light of the variability that is often observed in ι Her (see Table 1).

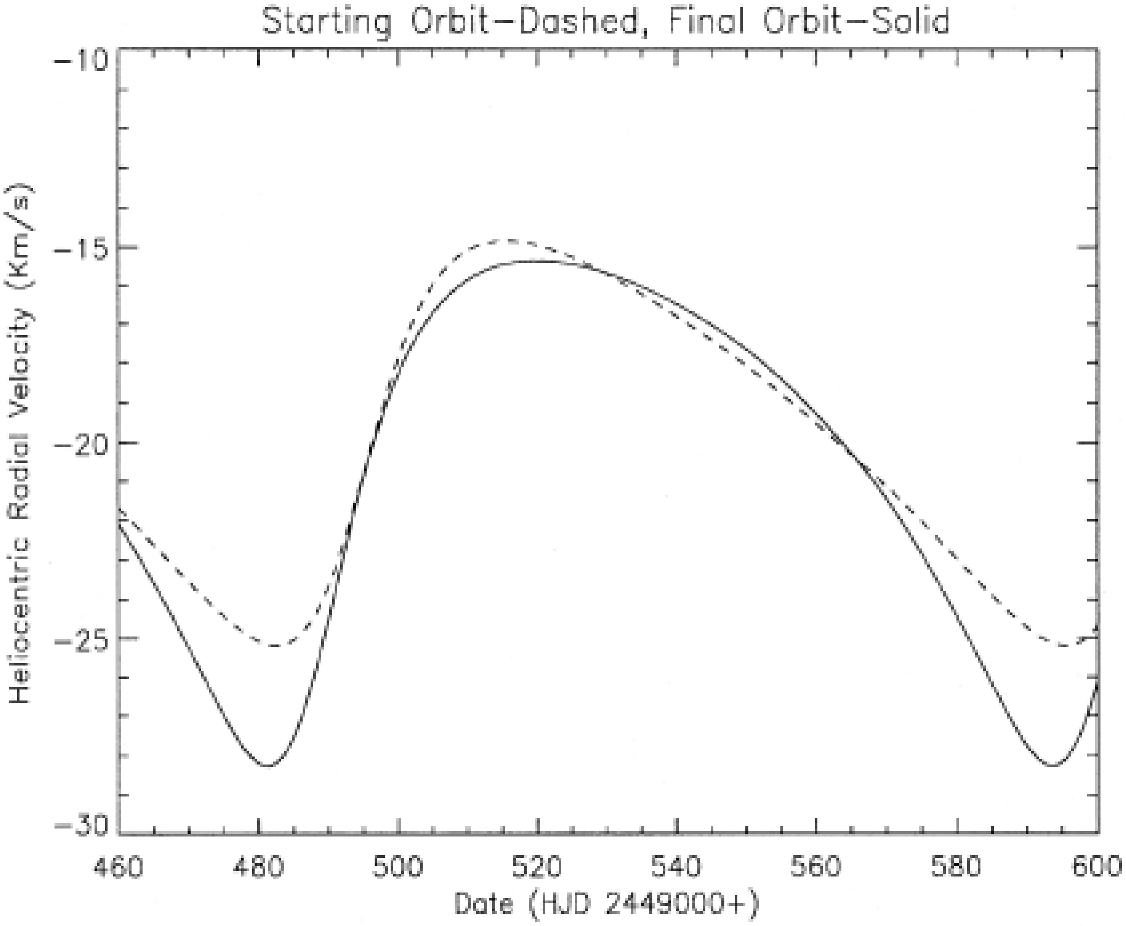

Fig. 7.— A comparison of the final orbit to the initial orbit.

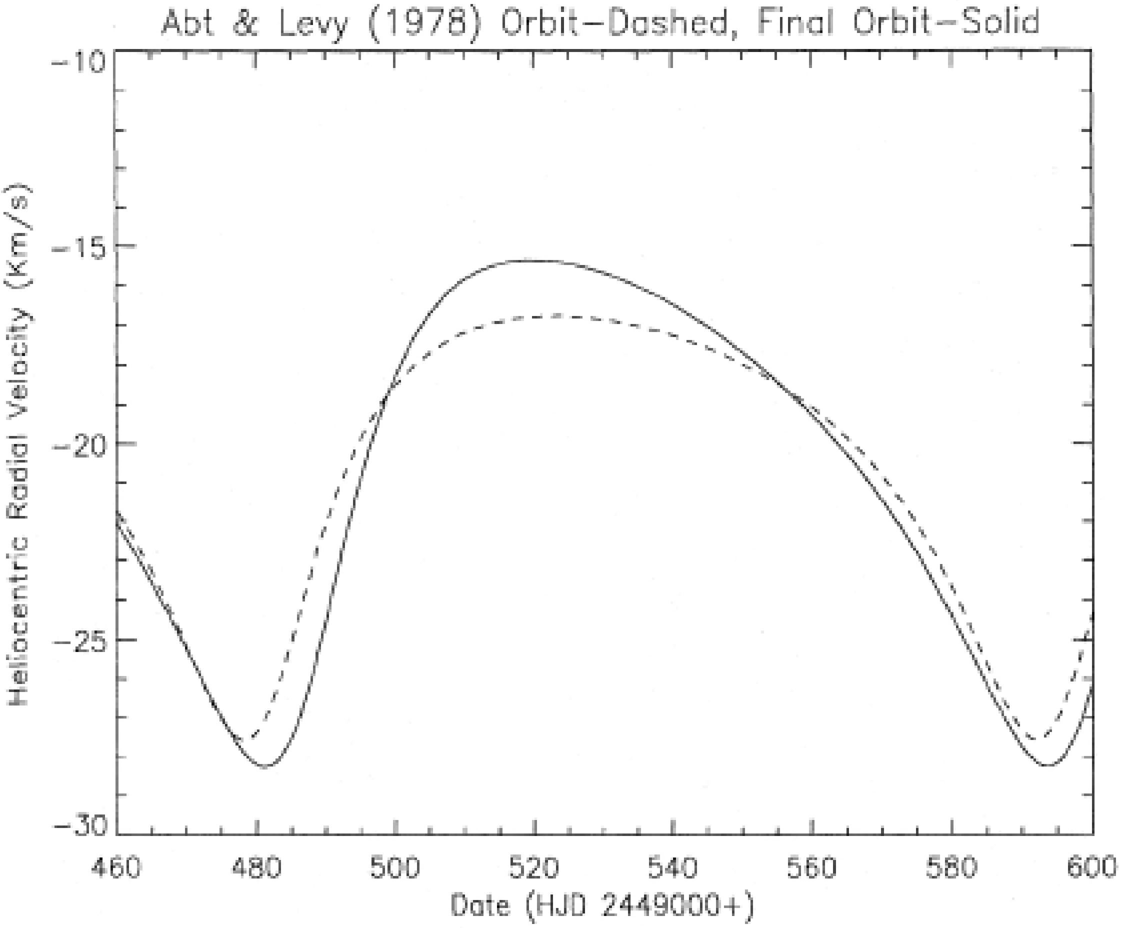

Fig. 8.— A comparison of the final orbit to the Abt & Levy (1978) orbit. The dashed line is the Abt & Levy (1978) orbit and the solid line is the orbit determined in this thesis.

2. Temporal Changes in Pulsation Modes

2.1. Background Information

One of the outstanding questions regarding pulsations (53 Per–type pulsations in particular) in early to mid B stars is the question of mode switching / mode growth. The current theory suggests that significant changes in an active pulsation mode should only occur on time scales much greater than a month; this is generally true of β Cep–type pulsations which are often observed to be stable for years to decades, but 53 Per–type pulsations have been observed to change modes (and amplitudes) on time scales as short as 1 day (Unno *et al.* 1989).

Changes in pulsation modes have often been observed in ι Her on many time scales including a month or less. Mathias & Waelkens (1995), for example, found that the amplitude of short period variations (1–1.5 hr) in the radial velocity of Si II lines changed by a factor as much as 4 from night to night. The fact that the different investigators in Table 1 have found greatly different pulsation periods and amplitudes based on different data sets also suggests the presence of mode switching, although it may also be partially explained by multiperiodic behavior (i.e. the data sets and different types of observations used by different investigators sample different time scales and/or different pulsation modes).

Perhaps the best example of mode switching in ι Her (prior to this work) can be seen in the work of Smith (1978). Smith obtained spectra of ι Her during 5 observing runs. For each observing run, he fitted theoretical models of pulsation modes to the profiles of absorption lines; he adjusted the assumed details of the pulsation modes until the best fit was obtained. Table 20 lists the modes that he identified as dominant.

Deriving pulsational properties from line profile fitting (the technique used by

Table 20: Mode Switching Seen By Smith (1978)

Observing Run	Range of Dates	Period of Pulsation Mode
Aug 3, 1976	Aug 3: UT 5:04 – 9:02	0.413 d
Mar, 1977	Mar 2 – Mar 4	0.413 d
Apr, 1977	Apr 23 – Apr 25	0.5792d
Jun/July 1977	Jun 30 – July 5	0.5792d
July/Aug 1977	July 27 – Aug 2	0.413 d

Smith 1978) often can be used to derive properties of only the dominant pulsation mode (Smith and Stern 1979). The term "mode switching" therefore refers to the situation where the role of dominant mode is transferred from one pulsational mode to another.

Table 20 shows that there are 51 days between the 2nd and 3rd observing runs where the mode was observed to switch from 0.413 days to 0.579 days. This new 0.579 day mode persisted for 74 days – 96 days before switching back to the 0.413 day mode in the 5th observing run. There are 23 days between the 4th and 5th observing run where the 0.579 day mode switched back to the 0.413 day mode. Thus, Smith's data suggest that the switching of modes occurs on a time scale of 23 – 51 days, with a given mode persisting for 74 – 96 days. While Smith's results suggest time scales, they are not well suited for the study of growth and decay of the pulsation modes. This problem will be addressed in the next section.

2.2. Sliding Window Analysis

In order to detect temporal changes in the pulsational characteristics in ι Her, the following technique was applied. A 30 datapoint wide window was slid along the radial velocity and W_λ data sets. At each window position, 30 consecutive points within the data set were analyzed. In the first window position the first 30 of the 58 observations were analyzed, in the second window position the 2nd through the 31st observations were analyzed, and so on.

At each window position, a Lomb periodogram was calculated; from it the dominant residual period was found. A Fourier–harmonic series was then fitted to the dominant period. For each window, the following quantities were calculated: the variance of the data (∇_1), the dominant period, the amplitude and phase in the fundamental term of the fit, and the variance after the Fourier–harmonic fit is subtracted (∇_2). The radial velocity data set was prewhitened by the final orbit solution before being analyzed. Thus the variance of the data refers to the variance in the orbit residuals, and the variance after the Fourier–harmonic fit refers to the variance after the Fourier–harmonic fit is subtracted from the orbit residuals. Figure 9 and Table 21 show the range of dates, arithmetic average HJD, and HJD at the midpoint for each window.

Each window covers a range that is typically around 80–100 days, and the difference between the average HJDs of adjacent windows is typically 3–4 days. Thus, the sliding window analysis is well suited to detecting the dominant mode in each window as well as the mode switching suggested by Smith's 1978 work. Recall that Smith found that a given pulsation mode was active for 74 to 96 days; this is just the range of dates covered in 1 window (with the exception of the first 2 and last 3 windows which coincide with large gaps in the data). Smith also found that switching of pulsation modes occurred on a time scale from 23 to 51 days; this

Table 21: The 30 Datapoint Wide Windows

	HJD (2449000.0+)		
Window	Average	Range	Midpoint
1	515.299	184.767	482.342
2	521.686	136.693	513.236
3	526.244	95.8113	533.697
4	529.438	90.8531	536.194
5	532.467	90.8602	536.208
6	535.496	89.8677	536.724
7	538.493	88.9939	537.198
8	541.895	100.954	544.274
9	545.260	99.0033	545.263
10	548.721	98.8538	550.169
11	552.018	97.9149	550.669
12	555.283	97.9603	550.700
13	558.679	101.864	552.661
14	562.075	96.9133	555.162
15	565.307	92.9121	557.187
16	568.405	92.9438	557.219
17	571.834	100.933	563.132
18	575.595	111.791	569.624
19	579.323	110.879	570.104
20	583.019	93.8948	578.620
21	586.150	91.9433	579.619
22	589.216	90.9856	580.122
23	592.249	80.9491	585.166
24	595.878	88.9563	609.068
25	598.844	88.8890	609.125
26	602.272	102.811	616.110
27	609.413	214.231	671.844
28	616.584	215.108	672.307
29	623.991	222.169	675.855

is considerably longer than the difference between the average HJDs of adjacent windows. Because the average width of a window is approximately the same as the duration over which a given mode was found to be dominant by Smith (1971), the results of each window are assumed to apply at the date given by the average HJD; this is somewhat analagous to the assigning the flux from a broadband photometric filter to the effective wavelength of the filter (Morrison 1995). At the same time, any changes in pulsational characteristics that occur on time scales much shorter than the typical range of 80–100 days will be averaged out by the window analysis.

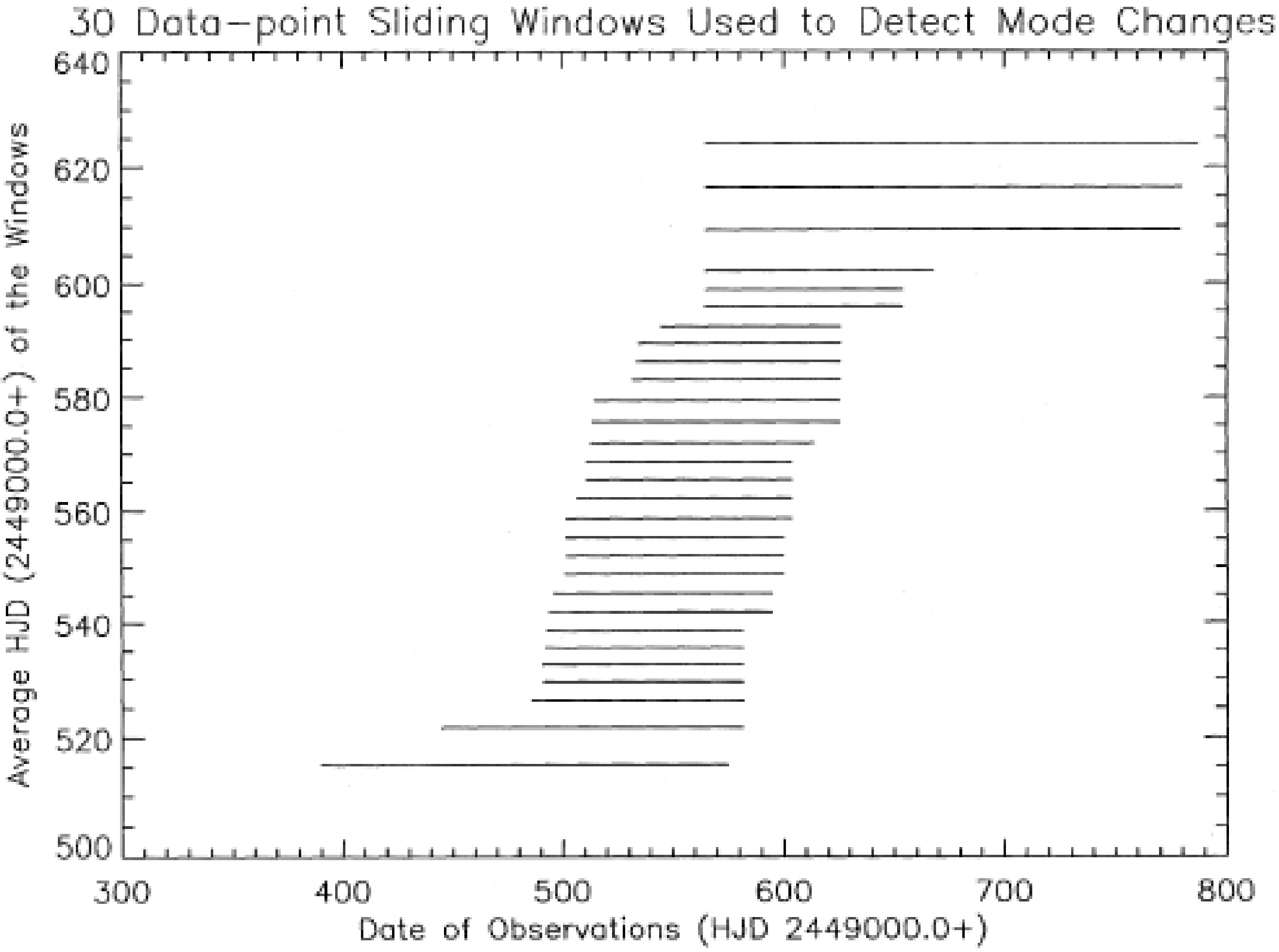

Fig. 9.— The sliding windows used to detect changes in pulsation. The horizontal lines indicate the width of each window.

The Radial Velocity Data

Table 22 shows that between the 18th and 19th windows (average HJD 575.595 and 579.323 respectively), the dominant pulsational period switched from 3.86d to 25–26d. The 3.86d mode was observed to decrease steadily in its amplitude from the first window until the 18th window. Likewise, the 25–26d mode was observed to increase steadily in amplitude from the 19th window to the last (29th) window. This behavior is demonstrated in Figure 10. The sliding window analysis also clearly demonstrates why the 3.86d radial velocity variation is the strongest in the total data set; it is active in most of the windows (18 of the 29) and its maximum amplitude is larger than that of the 25–26 day variation. An analysis of the 3.86d and the 25–26d modes as separate entities will be deferred until the next chapter; instead, the remainder of this subsection will discuss the changes in the pulsational characteristics of ι Her that are suggested by the sliding window analysis.

Table 22: Sliding Window Analysis of Radial Velocity Data

Window	Dominant Period(d)	∇_1 (km s^{-1})^2	∇_2* (km s^{-1})^2	Amplitude (km s^{-1})	Phase (rad)
1	3.853	3.05	1.60	2.7	0.964
2	3.853	3.47	1.55	2.8	0.998
3	3.853	3.62	1.29	2.7	0.950
4	3.877	3.41	0.87	2.5	–0.462
5	3.853	3.67	0.84	2.7	0.848
6	3.853	3.87	0.77	2.6	0.848
7	3.877	4.11	0.71	2.5	–0.519
8	3.877	3.62	0.71	2.4	–0.556
9	3.853	3.80	0.79	2.4	0.916
10	3.853	3.48	0.67	2.3	1.114
11	3.853	3.46	0.65	2.3	1.162
12	3.853	3.42	0.58	2.3	1.121
13	3.853	3.57	0.78	2.0	1.132
14	3.853	3.60	0.72	2.2	1.103
15	3.853	3.75	0.75	2.2	1.095
16	3.853	3.94	0.79	2.2	1.084
17	3.853	3.95	0.84	2.0	1.107
18	3.853	3.81	0.95	2.0	1.078
19	25.759	3.75	0.73	2.1	–0.466
20	25.903	3.75	0.72	2.1	–0.700
21	25.807	3.44	0.64	1.9	–0.608
22	25.278	3.44	0.47	2.3	0.599
23	25.278	3.15	0.78	2.2	0.335
24	25.302	3.24	0.67	2.6	0.317
25	25.542	3.20	0.56	2.4	–0.292
26	25.879	3.23	0.40	2.5	–0.853
27	26.047	3.35	0.42	2.5	–1.109
28	25.999	3.35	0.37	2.4	–1.060
29	26.479	3.35	0.39	2.5	1.154

* ∇_2 of 0.49 (km s^{-1})^2 is caused by the observational error.

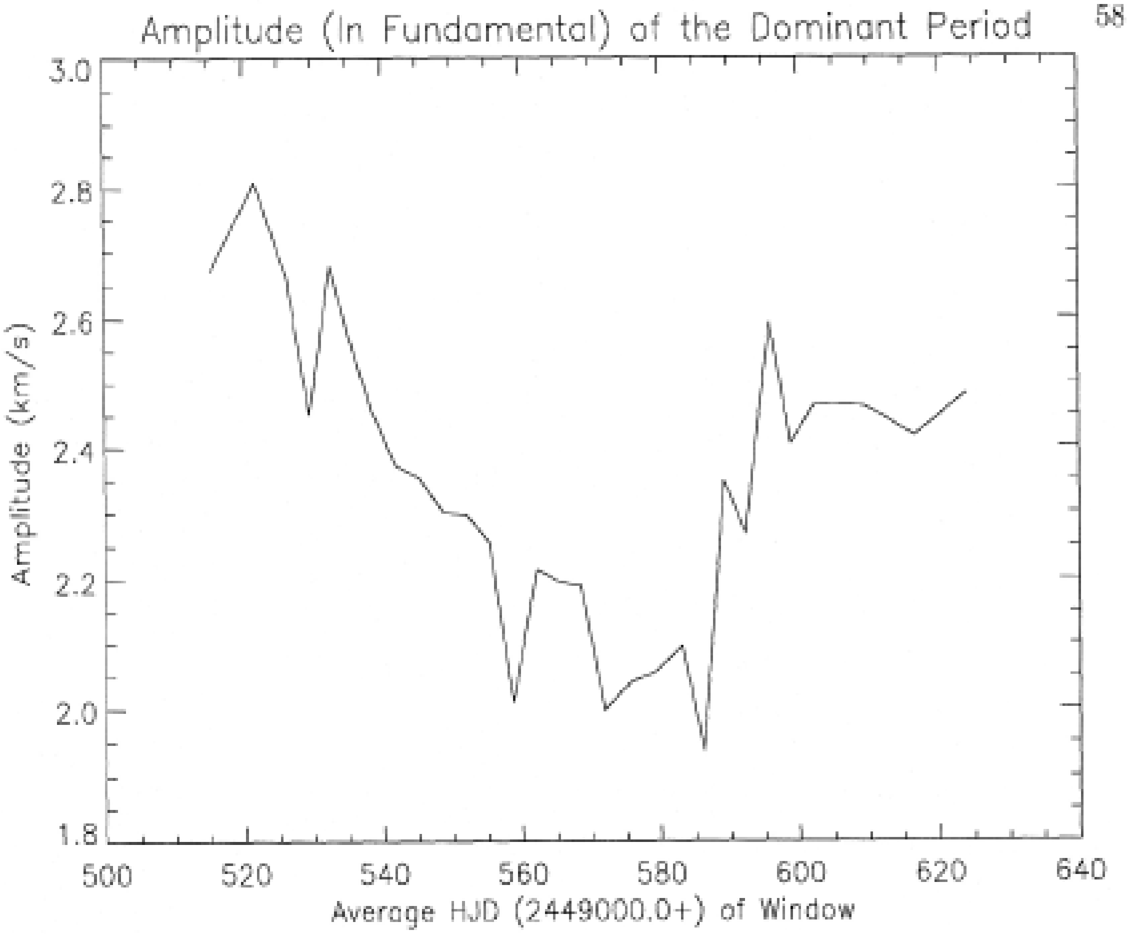

Fig. 10.— The amplitude of the dominant pulsation periods in the HRV data. The amplitude that corresponds to dates before HJD 575 is that of the 3.86d pulsation while the amplitude that corresponds to dates after HJD 579 is that of the 25–26d pulsation.

It is instructive to compare the time scale of changes seen in the data to those found by Smith (1978). Recall that Smith found that a given pulsation mode was dominant for a time scale of 74 – 96 days and that the transition from one mode being dominant to another mode lasted 23 – 51 days. The results of the sliding window analysis show that the 3.86d day mode was dominant but decreasing in amplitude for at least 60 days (the difference in average HJD between the 1st and 18th windows). The 25–26 day mode was dominant but increasing in amplitude for at least 45 days (the difference in average HJD between the 19th and 29th windows).

The transition between these two dominant modes occurred as the window moved from the 18th position to the 19th where the difference in the average HJD for the 18th and 19th windows was just 3.728 days.

Based on the data, it is tempting to speculate that the long–term behavior of pulsation modes in ι Her is such that the amplitude of modes increase and decrease over time as power is transferred from one mode to another; this causes the role of ‘dominant’ mode to be passed among a group of unstable modes. The duration of a given mode’s dominance was estimated by Smith (1978) to be 74 – 96 days, while the current observations suggest a time scale of at least 45 – 60 days. These time scales agree to with each other and the orbital period of 112 days within a factor of 2–3. That these time scales agree with one another suggests that mode switching occurs at regular intervals and that they be regulated by the binary motion. The possible relationship between binary motion and mode switching events seen in ι Her will be discussed in Chapter 5, Section 2 Currently, additional observations of ι Her are being accumulated in order to follow the development of its pulsational properties.

The Equivalent Width Data

In this subsection, the sliding window analysis of the equivalent width measurements of the S II (6) $\lambda5454$ line is presented. Only windows where the dominant W_λ variation has an amplitude greater than or equal to the observational error of 6 mÅ are shown.

Table 23: Sliding Window Analysis of W_λ Data

Window	Dominant Period(d)	∇_1 10^3 (mÅ)^2	∇_2* 10^3 (mÅ)^2	Amp (mÅ)	Phase (rad)	Comments
1	6.087	0.974	0.900	7	1.146	...
7	1.019	0.908	0.759	8	0.658	...
8	2.172	0.902	0.783	10	0.254	...
9	2.172	0.899	0.719	7	0.065	...
12	2.172	0.895	0.707	12	0.274	...
13	2.172	0.891	0.705	12	0.254	...
14	2.172	0.890	0.709	12	0.250	...
15	2.172	0.886	0.410	19	–0.556	...
16	12.956	0.890	0.570	9	0.247	...
18	0.538	0.877	0.836	6	0.562	...
19	0.538	0.878	0.829	6	0.563	...
20	0.538	0.880	0.830	6	0.563	...
21	6.855	0.885	0.543	7	–0.540	...
26	2.628	0.882	0.409	20	1.097	alias of 1.588d
27	6.423	0.883	0.447	7	–1.189	...
28	3.517	0.883	0.675	9	–1.529	alias of 0.80d

* ∇_2 of 36 (mÅ)^2 is caused by the observational error.

Unlike the radial velocity data, the W_λ variations are largely buried in noise. The ∇_2 variances in Table 23 correspond to observational errors of 20 – 30 mÅ. Either the error estimate of 6 mÅ is too small by a factor of 3 – 4 or there are variations (secondary to that caused by the dominant pulsation mode) that appear as noise to the analysis. The large uncertainties in the W_λ measurements must be considered in weighing the significance of the results described in this subsection. Table 23 shows a behavior that is markedly different from that of the radial velocity data. Whereas the radial velocity data show only two distinct periods (switching the role of dominant mode between window 18 and 19), the equivalent width data show that many different periods take the role of dominant W_λ variation. There is a fairly strong W_λ variation that was detected in window 26; this variation has an amplitude of 20 mÅ. The observed period in this window (2.628d ± 0.012) can be shown to be a 0.997d alias of 1.611d, the importance of which will be discussed in the next chapter.

Chapter 5

Results

1. Description of Individual Pulsation Modes

The sliding window analysis showed that the radial velocity data set consists of two distinct subsets (window 1–18 and 19–29), with the dominant mode in each subset having a period of 3.86d and 25–26 days respectively. The purpose of this section is to study the two pulsation modes separately.

1.1. The Radial Velocity Data

The 3.86d Pulsation Mode

Only two values of the period are found to be dominant in this subset: 3.853 and 3.877 days. These two values correspond to the same period within the uncertainty of the periodogram. The 3.853d value appears in 15 out of the 18 windows in the first subset while the 3.877d value appears in 3 out of the 18 windows. A weighted average of these values gives 3.857 ± 0.012 days as the value for the pulsation period.

The sliding window analysis also indicates that the period of the 3.86d mode is extremely stable, with any variations being less than the spacing of the Lomb periodogram. The phase that corresponds to the fundamental term in the Fourier–harmonic fit is also very stable (see Table 22). The phase does deviate from its ‘normal’ value for the 3 windows where 3.857d was assumed as the fundamental period; the average phase for these three windows in –0.512 radians. For the other 15 windows, the phase was very stable with an average value of 1.035 radians. This difference indicates a very sensitive dependence of the phase on the assumed period; the 0.024d spacing in the periodogram periods gave rise to a ± 1.547 radian error for the 3.86d period. The weighted average of the phase is 0.777 ± 1.547 radians; this value is taken as the phase of the 3.86d ± 0.01d period.

The sliding window analysis can also be used to investigate the possibility of other pulsation modes being active at the same time as the 3.86d period. This point is best illustrated by examining the variance in the data left over after the orbit and the fit to the 3.86d period have been subtracted (refer to Figure 11 and in Table 22 refer to the ∇_2 column). This variance is very high in the first window (at least several times that explained by the observational error in the data as estimated in Section 2.3), but it decreased until window 12 where it reached a point where most of the variance was accounted for by the observational error. This variance began to increase again until window 18 where the 24–26d mode became dominant. A possible interpretation of this behavior is that the excess variance above that due to the observational error was caused by additional pulsation modes.

During the time interval corresponding to the first 12 windows, a secondary pulsation mode was active but weaker than the 3.86d mode. This pulsation mode decreased in strength until the time corresponding to window 12 where it was no longer strong enough to be easily detected above the noise. Then, during the time interval corresponding to windows 13 through 18, the 25–26 day pulsation mode became

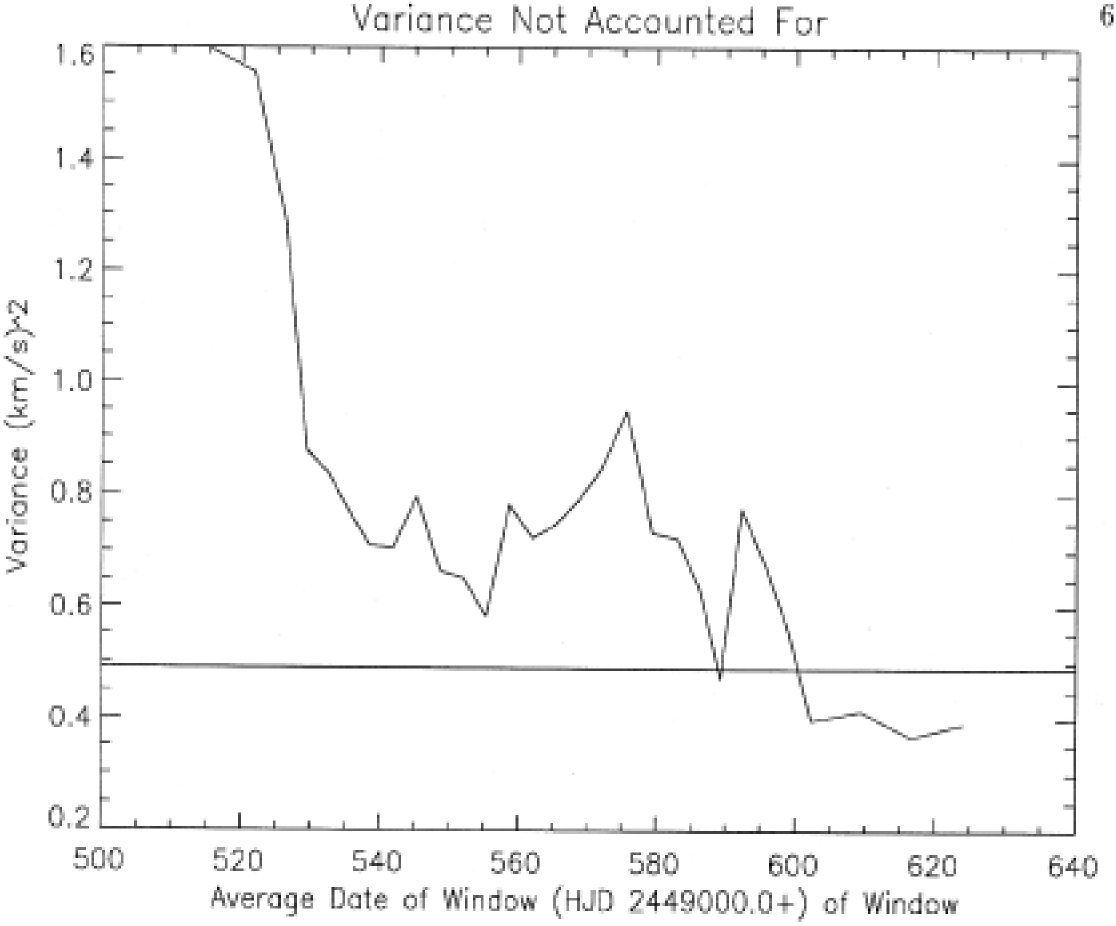

Fig. 11.— This variance is that which is left in the data after the orbit fit and fit to the dominant residual period are subtracted. The variance for each window is plotted against the average HJD of the window. The horizontal line indicates the variance due to the estimated observational error.

active but was weaker than the 3.86d mode. This pulsation mode increased in strength until it became the dominant pulsation mode in the data.

The amplitude of the 3.86d variations in the first sliding window is among the largest and the first sliding window most effectively isolates the 3.86d pulsation mode from the time when the 25–26 day mode that is dominant. For these reasons, the first sliding widow is studied in greater detail in the remainder of this section. The dominant peak in the periodogram of the 1st window has a period of 3.863 days while the second strongest peak had a period of 0.794 days (refer to Figure 12). The 3.863d period can be shown to an alias of the 0.997d (1 sidereal day) intrinsic sampling rate to produce a period of 0.794 days (refer to Appendix A.4). In other words, one of these two periods is real while the other one is an aliasing effect. There are several pieces of evidence that, when considered as a whole, indicate very

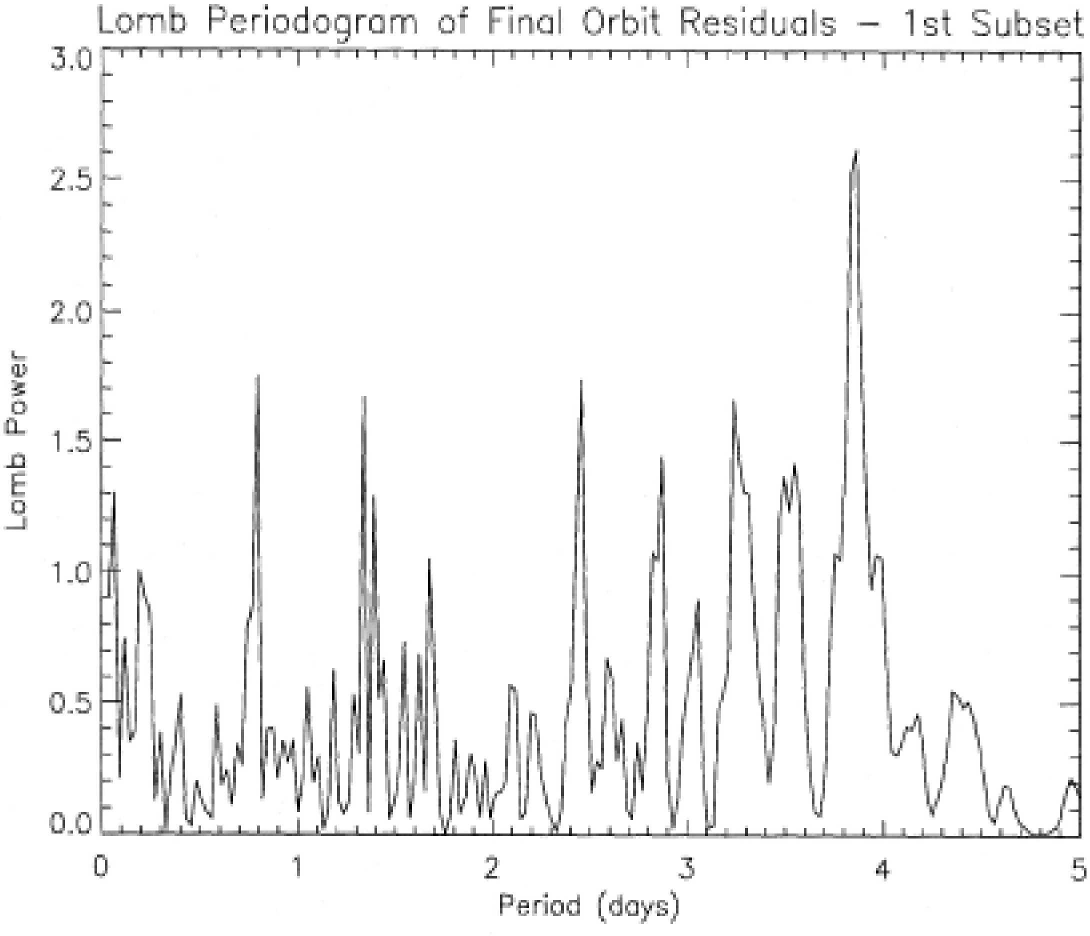

Fig. 12.— The Lomb periodogram of the 1st sliding window.

Evidence 1)

A Lomb periodogram was calculated from the radial velocities based on the blue observations alone, prewhitened for the orbit (refer to Figure 13). From Table 3, one can see that the blue observations are concentrated in groups taken on single nights, thereby sampling short–period oscillations as well as possible. In the periodogram of the blue data, the dominant peak has a period 0.818 ± 0.012 days; this value is identical to 0.794 ± 0.012 day within error. For the remainder of this work, the period of the 0.794/0.818 day period will be taken as 0.80 ± 0.01 days.

In a similar manner, the Lomb periodogram was taken of the red observations prewhitened for the orbit (refer to Figure 14). From Table 4, one can see that the red observations were typically taken 1 per night, thus maximizing the effect of the 0.997d aliasing. The dominant peak in this periodogram has a period of 3.86 days. Th fact that the more densely sampled data set yields the shorter period suggests that the 0.80d period is the physical one while 3.86d is the aliasing effect.

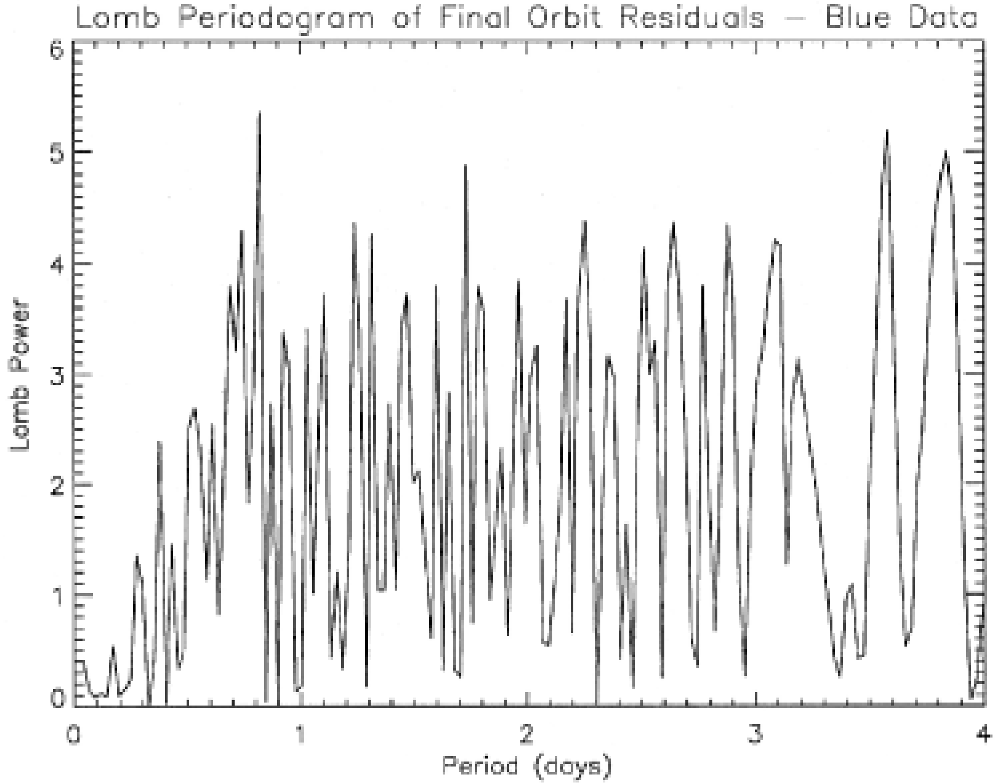

Fig. 13.— The Lomb periodogram of the final orbit residuals of blue observations.

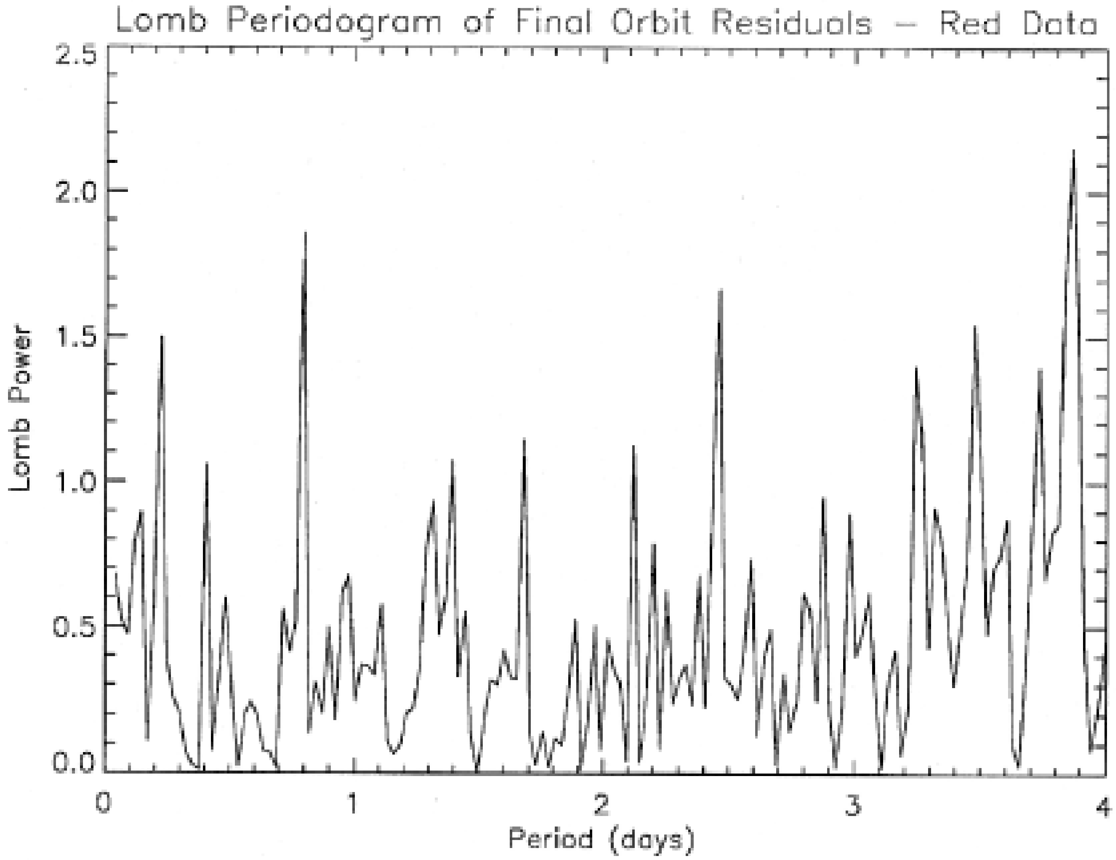

Fig. 14.— The Lomb periodogram of the final orbit residuals of red observations.

Evidence 2)

When the blue observations were prewhitened for the orbit and fitted by a Fourier– harmonic series with a period of 0.80d, the amplitude was virtually identical to that found when the red observations were prwehitened for the orbit and fitted by a Fourier–harmonic series with a period of 3.86d. As described in Appendix A, aliasing can be thought of as a interaction between a physically real period and a sampling rate in which the amplitude of the variability that is associated with the real period is conserved. The fact that the Fourier–harmonic fit to the 0.80d period in the blue data gives the same amplitude as the Fourier–harmonic fit to the 3.86d period in the red data strongly suggests that the two periods are related through aliasing.

Evidence 3)

In the Lomb periodogram taken of the 1st sliding window, there is a peak at 0.80d in addition to the strongest peak at 3.86d. This peak disappeared from the periodogram when the Fourier–harmonic fit to the 3.86d period was subtracted from the data. This fact strongly shows that only one of the periods is physically real; the first two pieces of evidence, in contrast, show only that the aliasing of the 0.8d period contributes to the 3.86d peak.

In summary, the 3rd piece of evidence shows that the periods are definitely related, the 1st and 2nd pieces of evidence show that they are almost certainly related through an aliasing effect, and the 1st piece of evidence strongly suggests that the 0.80d period is the real period while 3.86d is the aliasing effect. In addition, the 0.80d period is nearly an integer multiple of the 0.4125d variation that has been observed in ι Her before by Smith (1978); refer to Table 1. This fact lends physical reality to the 0.80d period. Because the evidence that the 3.86 day period is actually a 0.80 day period is highly suggestive but not absolutely conclusive, this pulsation mode will be referred to as the 3.86d (0.80d) mode in the remainder of this work. It should be noted that the amplitudes derived in Section 2.2 for the 3.86d pulsation are unchanged even if the 0.794d is the real pulsation period; see Appendix A.4). To examine the phase of the pulsation, should the real period be 0.80d instead of 3.86d, a Fourier–harmonic fit was made to the 1st window with the period 0.794d; the resulting phase was found to be –0.682 radians.

In order to investigate the possible secondary pulsation mode that may exist in the first subset of the data, the Fourier–harmonic fit to the 3.86d (0.80d) period were subtracted from the data in the 1st window. In the Lomb periodogram of these prewhitened data the dominant peak is 1.403 days. If the data are prewhitened for

0.794d instead, the dominant peak in the periodogram is 9.492 days; this period can be shown to alias with the 0.997d sampling rate to produce a period of 1.114 days, which is another strong peak in the periodogram. The secondary pulsation mode (if present) is likely to have a period of 1.114d or 1.403d, since 9.492 days is too long to be a pulsation in a star like ι Her; refer to Chapter 1. The period of 1.403d ± 0.012d, if it is the real secondary pulsation in the first subset, coincides within mutual error bars with the that was observed in ι Her by Mathias and Waelkens (1995).

The existence of a secondary period in the first subset can also be investigated by examining the variance associated with the 1st sliding window, which has the highest value of ∇_2 in Table 22. The variance between the S II radial velocities and the orbit fit was found to be 3.05 (km s^{-1})^2 in the first subset. The variance was reduced to 0.89 (km s^{-1})^2 and 1.37 (km s^{-1})^2 when the data for the first subset were prewhitened for the orbit and then the 3.86d and 0.80d periods respectively. The 3.86d (0.80d) period accounted for 70.8% (55.1%) of the variance in the orbit residuals whereas the observational error accounted for only 16.1% of the residual variance. Thus 13.1% – 28.8% of the residual variance is unaccounted for, indicating that a secondary pulsation mode was active in the 1st window. It was probably active early in the observations (where the ∇_2 in Table 22 is high) with a period of 1.114d or 1.403d (± 0.012d).

The 25–26d Pulsation Mode

The sliding window analysis of the second subset of the data (windows 19–29) shows that a (group of) pulsation mode(s) with a period that ranges from 25 – 26 days is dominant (refer to Table 22). Unlike the 3.86d (0.8d) period in the first subset, the dominant period shows somewhat erratic behavior with a period ranging from 25.278 to 26.479 days. Although the periodic variation that is seen is likely due to the interaction of 2 or more modes, it will be referred to as the "25–26d mode" in the remainder of this work.

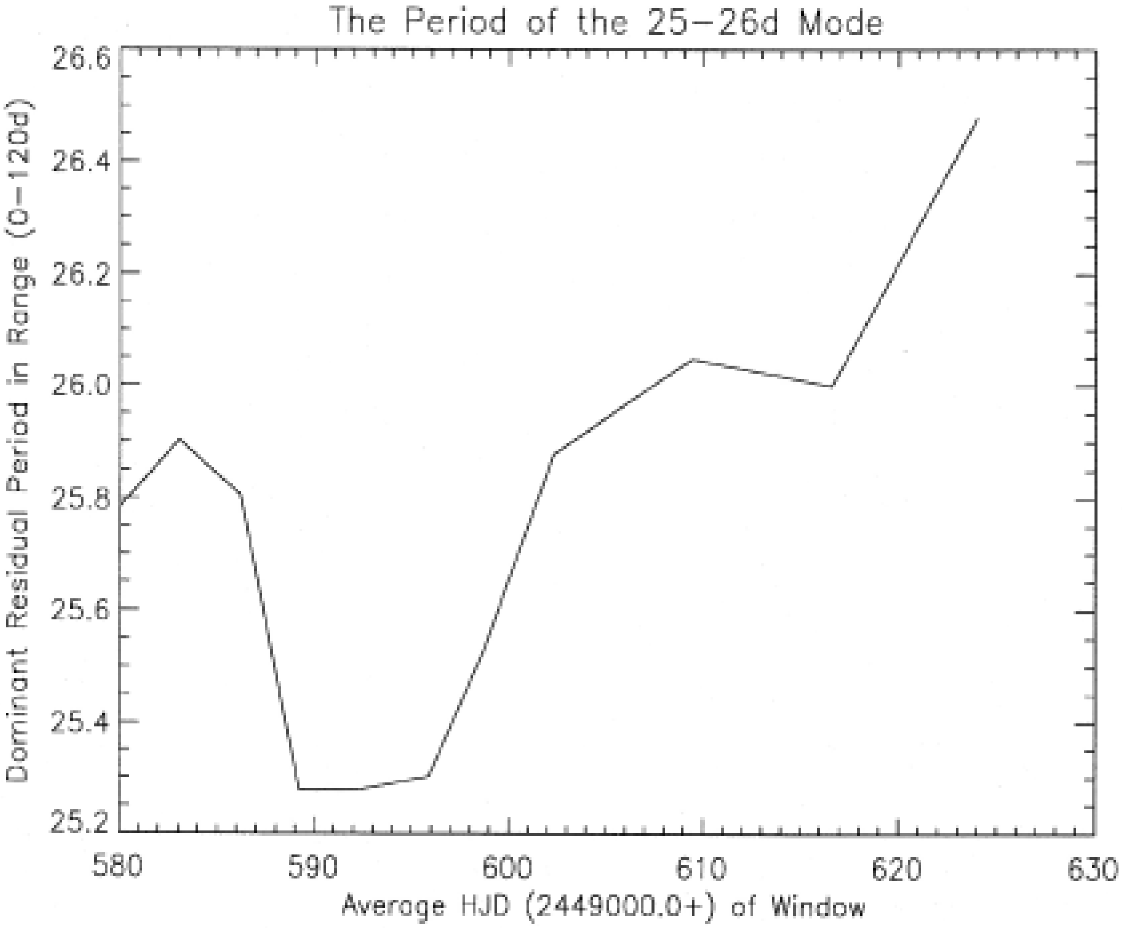

Fig. 15.— The dominant periods (25–26d) in the second subset of the HRV data.

The sliding window analysis may also show evidence that the 3.86d (0.80d) pulsation mode exists into the second subset of data where the 25 – 26d mode dominates. This can be seen by looking at the variance in the data after the orbit and the Fourier–harmonic fit to the dominant period have been subtracted out (refer to Figure 11 and in Table 22, the ∇_2 column). This variance starts out with a value of 0.73 (km $s^{-1})^2$ at window 19 and decreases to 0.39 (km $s^{-1})^2$ by window 29. By the last window, the variance is clearly at the level indicative of only noise due to observational error. There may, however, be a secondary pulsation active in the first part of the second subset (window 19 – 24), which may be the 3.86d (0.80d) mode as its amplitude decreases below the detection level.

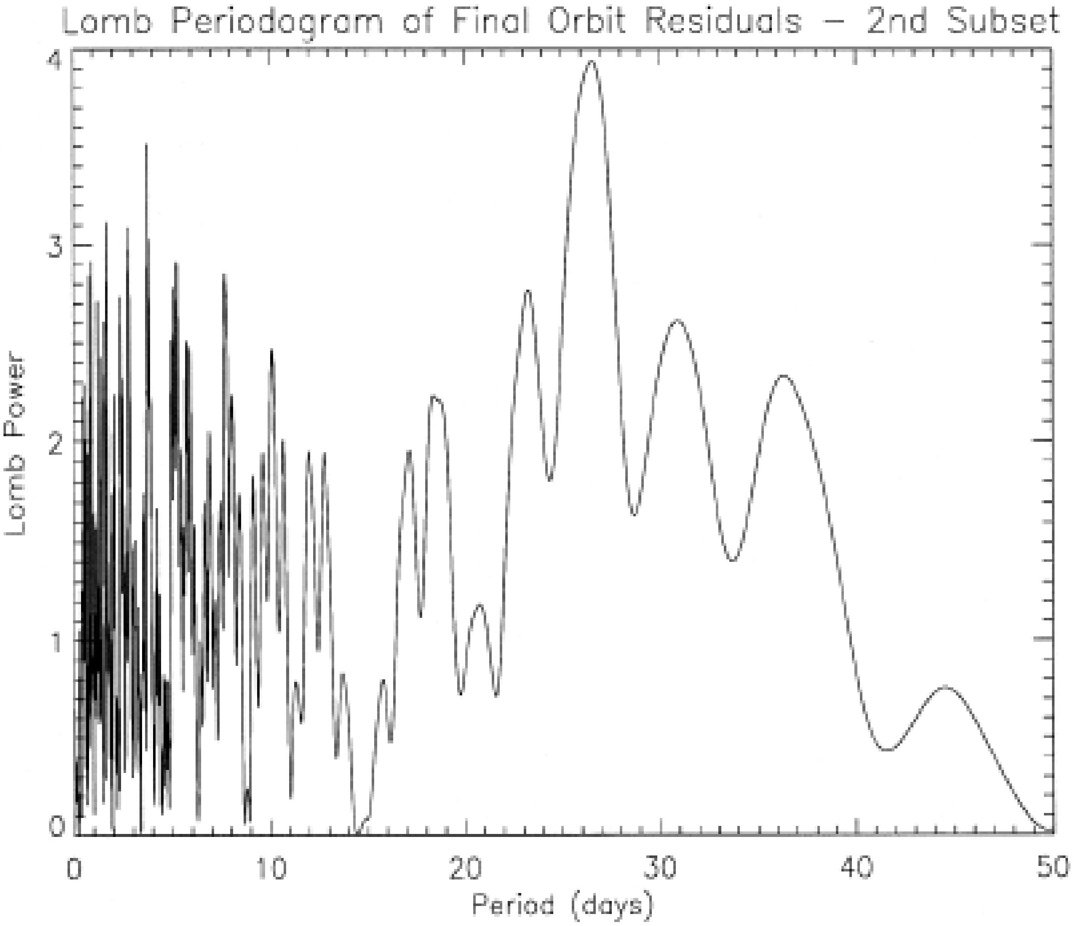

Fig. 16.— The Lomb periodogram of the final orbit residuals for the second subset of the HRV data.

A 25–26d periodicity in ι Her has already been predicted by Rogerson (1984), who found two pulsation modes occurring simultaneously but with slightly different radial velocity amplitudes (refer to Table 1) in observations taken with the Copernicus spectrophotometer in May 1979. Rogerson found that the periods of these two pulsation modes were 1.515 and 1.618 days ± 0.021 days. The beat period corresponding to these two periods is 23.799 days. Given the errors stated by Rogerson, the beat period may be as short as 18 days or as long as 40 days, a range that comfortably includes the 25–26 day periods that are observed.

The sliding window analysis suggests that the two modes observed by Rogerson are active in our data and that they beat to produce the 25–26d pulsation that dominates the second subset of the data. In the Lomb periodograms for the second subset of the data, peaks with periods around 1.515d and 1.618d are present. In Table 24, the dominant periods from the window periodograms are listed in three ranges of date: the period in the range of 1.44d–1.55d, the strongest in the range of 1.55d–1.65d, and the strongest overall.

Table 24: Evidence for Rogerson's Periods

	Dominant Period in the Range of		
Window	1.45–1.55d	1.55–1.65d	Dominant Period
19	1.525	1.573	25.759
20	1.525	1.573	25.903
21	1.525	1.573	25.807
22	1.525	1.573	25.278
23	1.525	1.597	25.278
24	1.525	1.597	25.302
25	1.525	1.597	25.542
26	1.525	1.597	25.879
27	1.549	1.597	26.047
28	1.549	1.597	25.999
29	1.549	1.597	26.479

The 2 values found for the strongest period in the range of 1.44d–1.55d are identical to within the 0.024d spacing and have a weighted average of 1.532 ± 0.012 days. The 2 values found for the strongest period in the range of 1.55d–1.65d are also identical to within the 0.024d spacing and have a weighted average of 1.588 ± 0.012 days. The uncertainty in periods taken from the Lomb periodogram makes it possible for two periodic variations to exist, beat to produce the dominant period that is observed in the 25 – 26 day range, and be registered by the periodogram as having the periods 1.532 and 1.588 days.

The fact that Rogerson found that his two modes had different amplitudes has a direct and important implication. If two periods (P_1 and P_2) are beating with one another with different amplitudes (A_1 and A_2), then the sum of their periodic

variations cannot be replaced by a single sine function with a period equal to the beat period. Instead, the sum of the two periodic variations consists of three terms as follows. Let P_b be the period of the beat which equals $(P_1^{-1} - P_2^{-1})^{-1}$. Let A be the average amplitude of the beating variations which equals $(A_1 + A_2) / 2$. The sum of the variations $(F_1(\mathrm{t}) + F_2(\mathrm{t}))$ is then given by
$F_1(t) + F_2(t) = Asin(2\pi tP_b) + (A_1 - A)sin(2\pi tP_1) + (A_2 - A)sin(2\pi tP_2)$
where each sin term has a phase that has been omitted.

In other words, because the amplitudes of the two Rogerson periods are (or can be) different, the data should show the strongest periodicity at the beat period as well as weaker periodicities at the two beating periods. The data show just such a behavior. The periods 1.532 and 1.588 days are identical to the two Rogerson periods (1.515 and 1.618 days) within mutual errors (0.012d in the current work and 0.021d in Rogerson's periods). Thus, the data confirm the existence of the periods reported by Rogerson (1984) as well as the predicted beat.

1.2. The Equivalent Width Data

Lomb periodograms were calculated for the equivalent width data as above, except that, of course, a 112d orbital variation was not removed.

The 3.86d (0.80d) Pulsation Mode

There is no significant detection of the 3.86d (0.80) pulsation mode in the windows where that mode dominated the radial velocity variations. This implies that the 3.86d (0.80d) mode is not strongly associated with variations in W_λ above the noise level of 6 mÅ. There is one window in the later part of the observations where a 0.997d alias of 0.80d ± 0.012d may dominate the W_λ variations (window 28).

The 25–26d Pulsation Mode

In the observations, window 26 has the Rogerson 1.588d ± 0.012d period as dominant. The dominant period in this window is 2.628d ± 0.012d which can be shown to be a 0.997d alias of 1.588d ± 0.012d. The fact that the radial velocity variations associated with the Rogerson periods have a maximum amplitude at window 24, whose average HJD is very close to that of window 26, suggests that the W_λ variations in window 26 are associated with the Rogerson 1.588d period.

This analysis of the second subset shows that the 1.532d Rogerson period never dominates the W_λ variations. If the amplitudes of the two Rogerson modes scale together, then the amplitude of W_λ variations associated with the 1.532d mode must always be much smaller than that associated with the 1.588d; if they were of comparable amplitudes, then a 25–26d periodicity would have been detected in the W_λ variations.

2. A Possible Cause for Mode Switching in ι Her

Section 2 describes the two mode switching events that Smith (1978) observed in his radial velocity data and the mode switching event that is studied in this work. This section will offer a possible explanation for the mechanism that triggers the mode switching: tidal interaction between the ι Her and its companion at periastron.

Table 25 shows ranges of dates when mode switching has been reported in ι Her, the date of the closest periastron passage, and Δ, which is the absolute value of the difference bewteen the switch and the closest periastron. The reported cases of mode switching in the radial velocity variations of ι Her all occur very close to a periastron passage.

Table 25: Mode Switching at Periastron

Work	Mode Switch	HJD (2440000.0+) of Closest Periastron Passage	Δ(days)
Smith (1978)	2933 – 2956	2970	14
Smith (1978)	3205 – 3256	3192	13
This Thesis	9576 – 9579	9599	20

The binary orbit solution (refer to Section 1) clearly indicates that the orbit is highly eccentric (e=0.38 ± 0.04). The separation at periastron of components in an eccentric orbit is less than the separation at apastron by a factor of (1 + e)/(1 –e). For the ι Her system, the separation at periastron is a factor of 2.23 smaller than it is at apastron. The disruption of the primary's surface by tidal forces in a binary system is approximately inversely proportional to the separation distance to the third power (Shore *et al.* 1994). Thus, the tidal disruption at periastron is a factor of 11.09 greater than it is at apastron. If an interaction between the ι Her and its companion is the cause of the mode switching, then the mode switching should occur near or at periastron passages because the tidal forces temporarily alter the internal structure of the star which, in turn, affects the pulsational characteristics.

The probability that the mode switching has nothing to do with the binary orbit and occurs by chance within X days of the periastron passage is 2X/P, where P is the 112.36 day orbital period; this gives a false alarm probability. Considering each mode switch as a statistically independent event, the false alarm probability of detecting 3 mode switchings within 13, 14, and 20 days of periastron passages is the product of the false alarm probabilities for the three mode switchings; this value is 2%. Although the observations in this work span several orbital cycles, the difference between the average HJD of the first and last sliding window only spans 1 orbital cycle. The sliding window analysis, therefore, covers only 1 periastron passage, and the analysis includes no periastron passages where mode switching was not observed.

Based on this low false alarm probability, it is plausible that the mode switching is triggered by tidal interaction at periastron passage. If tidal interactions are the cause of mode switchings, then any given pulsation mode should persist for a length of time comparable to the orbital period of 112.36 days. Smith (1978) observed pulsations to dominate for 74 – 96 days before switching and the current work suggests time scales of at least 45 – 60 days; these time scales are consistent with the orbital period of 112.36 days. While the evidence is not conclusive, it suggests that the hypothesis of tidal interactions at periastron triggering the mode switching events is worthy of further investigation.

Chapter 6

Conclusions

This thesis has identified the radial velocity periodicities in ι Her that are caused by pulsations, as indicated by variations in the S II (6) λ5453.810 line. Measurements of that line's equivalent width and line asymmetry were studied as well in order to describe the nature of velocity variations (i.e. were they accompanied by equivalent width variations?). Particular attention has been paid to the temporal changes that the observed pulsation modes experienced during the course of the observations. The purpose of this section is to summarize the results.

This work has identified a previously unreported radial velocity variation with a period of 0.80d ± 0.01d. This work has also confirmed the two periodicities cited by Rogerson (1984): 1.515d and 1.618d ± 0.021d. These periodicities and their beat were observed in the radial velocity variations of the S II λ5454 line to have the periods of 1.532, 1.588, and 26.565 ± 0.012 respectively. The two periods and their beat were observed in radial velocity data, while the 1.588d periodicity was also observed in a subset of the equivalent width data.

The most significant result of this work was the detection of long–term trends in the amplitudes of radial velocity variations, including the occurrence of mode switching where the role of dominant velocity variation changed from one mode to another. In the first 30 of the 58 observations, the dominant radial velocity variation had a period of 0.80d. The amplitude of this velocity variation was observed to decrease steadily over a interval of 60 days until the role of dominant velocity variation was observed to switch to the beat between the Rogerson periods. In the last 28 of the 58 observations, the amplitude of 25–26d beat was observed to increase steadily over a interval of at least 45 days. The mode switching event that is described in this work occurred near the time of periastron passage; this result suggests that tidal interactions at periastron perturb the internal structure of ι Her causing the mode switching to occur.

If the above picture is correct, then it may explain why different observers see different modes active at different times or the same mode active but with different amplitudes. While mode switching has been detected before in ι Her (Smith 1978), this work presents the first description of the decay and growth of the modes over long time scales as well as a possible explanation for the cause of the mode switching. Mode switching is inherently a non–linear phenomenon (Unno *et al.* 1989) because power is being transferred between two different unstable pulsation modes. The full non–linear theory of non–radial pulsations is just now beginning to be studied and applied to pulsating B stars (Goupil & Buchler 1994; Van Hoolst 1994; Moskalik & Buchler 1994). The observed instance of mode switching that is described in this work may serve as an observational constraint for the newest generation of non–linear, non–radial pulsation models.

Table 26 summarizes the observed properties of the two pulsation modes that were observed to dominate the radial velocity variations: the 3.86d (0.80d) mode and the 25–26d mode. For the radial velocity variations, the table displays the smallest, average (in parentheses), and largest amplitudes that were observed in the window analysis. The table also points out any long term trends that exist in the measurements.

Table 26: Properties of Pulsation Modes

Period	RV Variations Amplitude(km s^{-1})	W_λ Variations Amplitude(mÅ)
0.80d	2.0 (2.4) 2.9	9
Trend	Decreasing	Indeterminate
25–26d	1.9 (2.3) 2.6	Not Observed
Trend	Increasing	Indeterminate
1.532d	< (2.3)	<< 20
Trend	Increasing	Indeterminate
1.588d	< (2.3)	20
Trend	Increasing	Indeterminate

From Table 26, the properties of the two pulsation modes can be compared. The first mode (period of 0.80d) was accompanied by relatively small equivalent width variations. The 1.588d period (part of the 25–26d 'mode') is accompanied by large equivalent width variations, but only near the time interval when the 25–26d period had its maximum radial velocity amplitude. Changes in the equivalent widths of optical Si II and Si III lines in ι Her have been studied by Smith (1978). Smith found that such variations were not consistent with temperature variations in the star's atmosphere. Instead, he showed that the variations could be caused by variations in the microturbulent velocity field within the star. It is very likely that the equivalent width variations in the strong S II line are due to the same mechanism.

As a byproduct of this work, a revised orbit was obtained for ι Her. This orbit is based on radial velocity data of a higher quality and at least as great a quantity than those used in previous orbit determinations. Additionally, the orbit was calculated in a way that takes into account the strongest radial velocity variation due to pulsations in the overall data set.

Finally, the velocity data show that different pulsation modes can be dominant at different times; the first half of the observations were dominated by a 0.80d velocity variation whereas the second half of the observations were dominated by a 26.565d period (a beat between the two Rogerson (1984) periods). The first part of the velocity data also showed evidence of a secondary pulsation period (besides the 0.80d period), accounting for 13.1% – 28.8% of variance in the orbit residuals. This secondary pulsation had a velocity variation with a period of 1.114d or 1.403d ± 0.012d. The periods associated with all of the observed periods that are dominant in the radial velocity data (0.80d, 1.532d, and 1.588d ± 0.012d) are in the range appropriate for 53 Per (or SPB) non–radial pulsations. Thus, by the strictest definition, the results do not place ι Her into the class of β Cep stars.

A. The Lomb (Scargle) Periodogram

Throughout this work, data are being searched for periodic variations. The data are, however, sampled unevenly with respect to time: this fact makes conventional Fourier–transform power spectra somewhat invalid. A technique that is designed for unevenly spaced data is the Lomb (Scargle) periodogram (Lomb 1976, Scargle 1982) because it weights the time of each observation and not the time interval between observations.

In this appendix, the basic concepts of the Lomb periodogram will be described with emphasis comparing it to the Fourier–transform based power spectrum. The following description is based on the work of Scargle (1982).

A.1. Definition of the Lomb periodogram

Given the following:

N = Number of data points
t(i) = Time of observations
X(i) = X(t(i)) Value of the observations
X_m = Mean value of X(i)
V = Sample variance

The sample variance (V) is:

$$V = \frac{1}{N-1} \times \sum_{i=1}^{N} (X(i) - X_m)^2$$

Let $\tau = \tau(\omega)$ = a constant as a function of angular frequency (ω).

$$Tan(2\omega\tau(\omega)) = \frac{\sum_{i=1}^{N} sin(2\omega t(i))}{\sum_{i=1}^{N} cos(2\omega t(i))}$$

Let P = P(ω) = Lomb power as a function of angular frequency (ω).

$$P = \frac{1}{2V}\frac{\left[\sum_{i=1}^{N}(X(i)-X_m)cos(\omega t(i)-\omega\tau(\omega))\right]^2}{\sum_{i=1}^{N}\left[cos^2(\omega t(i)-\omega\tau(\omega))\right]}$$
$$+\frac{1}{2V}\frac{\left[\sum_{i=1}^{N}(X(i)-X_m)sin(\omega t(i)-\omega\tau(\omega))\right]^2}{\sum_{i=1}^{N}\left[sin^2(\omega t(i)-\omega\tau(\omega))\right]}$$

The above mathematical framework was implemented (by the author) in an IDL routine.

A.2. A more intuitive definition for the Lomb periodogram

The expression for the Lomb power P(ω) can be derived from a standard linear least–squares treatment; this will give a more intuitive understanding of what the Lomb power physically represents.

Assume that the following model describes the data.

$$X_f(i) = A\ cos[\omega t(i)-\omega\tau(\omega))] + B\ sin[\omega t(i)-\omega\tau(\omega))]$$

The best fit of such a function (at every frequency) can be obtained by minimizing the sum of the square of the differences (errors) between the observed data and the fitting function with respect to A and B; ie. to minimize the following:

$$S.S.E.(w) = \sum_{i=1}^{N}(X_f(i)-X(i))^2$$

One can select $\tau(\omega)$ so as to eliminate a cross term that arises in the product (X_f(i)–X(i))^2; this choice of $\tau(\omega)$ is identical to that previously defined.

Finally, one may define the "reduction in the sum of squares" at a given frequency as: R.S.S.E.(ω) = $\sum_{i=1}^{N} X(i)^2$ – MIN [S.S.E.(ω)] with respect to A and B. One can easily show that the Lomb power is exactly equal to the reduction in the sum of squares (R.S.S.E.) normalized (i.e. divided) by the variance (V).

The Lomb periodogram can, thus, be thought of as a procedure that fits (at each frequency) a general trigonometric function (i.e. X_f) to the data. The Lomb power at a frequency measures how well the general trigonometric function (at its least–squares best) can be made to fit the data.

A.3. Statistical properties of the Lomb periodogram

This section will describe how the power level in the Lomb periodogram is affected by purely random, mean–zero, Gaussian distributed noise.

The probability for finding P (at any given frequency) due to noise in the range P=Z to P=Z+dZ is given by:

$$Prob(Z)dZ = e^{-Z}dZ.$$

The probability that the power P (caused by noise) is greater than and less than a specific power level Z_o are given by:

$$Prob(Z > Z_o) = e^{-Z_o} \ and \ Prob(Z < Z_o) = 1 - e^{-Z_o}.$$

These results indicate that the likelihood of a peak in the periodogram with power P(ω)=Z_o being due to noise decreases exponentially with the Lomb Power level (Z_o); thus a peak that extends just slightly above the continuum of the Lomb power spectrum may, in reality, be a very significant signal in the data. The significance level of a peak in the Lomb periodogram can be a very complicated function of frequency due to the unevenly spaced nature of the data and there are methods for estimating the significance based on the Lomb power of a given peak. In this work, the significance of peaks in periodograms are estimated in a much more straightforward and intuitive manner. The variance in a data set is calculated, a Fourier–harmonic fit is made using the period that corresponds to the peak of interest as the fundamental, the fit is subtracted from the data, and the variance in the new data set is calculated. The difference of the two variances is a measure of the "significance" of the peak. This method measures the significance of the period and its harmonics, while the Lomb power measures only the significance of the fundamental period.

A.4. Advantages and disadvantages over a power spectrum

The main advantage of the Lomb periodogram is the fact that it is designed to work with unevenly spaced data. The fact that the data are unevenly sampled gives rise to an important benefit over the power spectrum: the data can yield periodicities with frequencies well above the Nyquist frequency because the time scale that limits detection is not the average time between observations, but the minimum time between observations.

A secondary advantage is the fact that if the data are unevenly spaced enough to call for a Lomb periodogram, then they are likely to be uneven enough to eliminate most aliasing problems. Astronomical observations are, however, very strongly aliased by the intrinsic sampling rate of 0.997 days (1 sidereal day) which may not be removed even in highly uneven data. Any aliasing that occurs with the intrinsic sampling rate will conserve the amplitude of the real oscillation (a beat between two real oscillations will add the amplitudes of the beating oscillations). If two frequencies are present in the data ($f_1 and f_2$) and are related through aliasing with the 0.997d sampling rate, it may not be possible to determined which is real and which is the alias; but, the amplitude derived from a Fourier–harmonic fit to the 2 frequencies will be identical. Thus, even though there may be some ambiguity in the frequency of an oscillation, its amplitude can be always be determined.

The main disadvantage in the Lomb periodogram is the fact that different frequencies are no longer orthogonal to one another as they are in a power spectrum because a discrete summation over a sine (or cosine) function with unevenly spaced data does not yield the orthogonality that exists in a discreet summation with evenly spaced data.

The fact that frequencies are not orthogonal means that they can be inter–related in a complicated manner. The most practical way to deal with this problem is called ‘prewhitening’. Consider a Lomb periodogram that displays peaks at 2 different frequencies, with frequency f_1 being the strongest. In order to be sure that the other frequency (f_2) is independent of f_1; one must fit a periodic function with a frequency of f_1 to the data and then subtract this fit from the data. This subtraction process in the time domain is called prewhitening. Only if the frequency (f_2) is still present in the Lomb periodogram of the data after the data has been prewhitened for the f_1 frequency, can it be considered as real and independent of frequency f_1.

B. Uncertainties in W_λ and Line Asymmetry Measurements

In this thesis, measurements of the equivalent width and line asymmetry of the S II λ5454 line are studied in an attempt to describe the physical nature of pulsation modes that are seen in the radial velocity measurements. While these measurements are only used as supporting data, it is (none the less) important to know the uncertainty in these measurements so that the results based on them can be fully interpreted. This appendix will derive a formula for the uncertainty in W_λ and line asymmetry measurements that stem from the uncertainty of continuum placement.

Basic definitions

W_λ = the equivalent width rendered from a continuum normalized spectrum.

F_c= the flux at the local continuum of the absorption line being measured. Because the W_λ's used in this thesis are measured from continuum normalized spectra, the value of F_c will be approximately 1.0 in all cases.

W_o = the wavelength which bisects the line profile at F_c.

W = the total width of an absorption line at the local continuum (F_c).

W(lhs) = the width of an absorption line (measured at F_c) from the line minimum to the short wavelength (i.e. left hand side) terminus of the line.

W(rhs) = the width of an absorption line (measured at F_c) from the line minimum to the long wavelength (i.e. right hand side) terminus of the line.

E+ = the amount (in units of normalized flux) that the local continuum can be raised before becoming obviously too high (by eye).

E– = the amount (in units of normalized flux) that the local continuum can be lowered before becoming obviously too low (by eye).

E = the average uncertainty in the continuum placement = 0.5 × (E+ + E–).

f(wl) = a function that describes the absorption line profile as a function of wavelength (wl).

The mathematical definition of an equivalent width is:

$$W_\lambda \ = \frac{1}{F_c} \int_{W_o - W(lhs)}^{W_o + W(rhs)} [F_c - f(wl)] \ d(wl)$$

which is equal to

$$W_\lambda \ = W - \int_{W_o - W(lhs)}^{W_o + W(rhs)} [f(wl)/F_c] \ d(wl)$$

The derivation

With the above definitions, it is now possible to derive the error in the W_λ and line asymmetry measurements that are caused by an uncertainty in the placement of the local continuum. The derived uncertainty will be the same for the W_λ measurements as the line asymmetry measurements; the derivation will be done for the W_λ measurements and then shown to be applicable to the line asymmetry measurements.

Step 1) Differentiate W_λ with respect to F_c.

The differentiation results in three terms.

$$\frac{d(W_\lambda)}{d(F_c)} = \left[\frac{d(W(rhs))}{d(F_c)} - \frac{d(W(lhs))}{d(F_c)} \right]$$

$$+\frac{1}{F_c}\left[W - W_\lambda\right]$$

$$-\frac{1}{F_c}\left[f(W_o + W(rhs))\frac{d(W(rhs))}{d(F_c)} - f(W_o - W(lhs))\frac{d(W(lhs))}{d(F_c)}\right]$$

Step 2) Eliminate terms.

While the formal differentiation contains three terms, in practice, only the second term contributes to the uncertainty in W_λ caused by the placement uncertainty in the continuum. This fact can be justified in two ways.

(1) The right and left terminus of the line profile are generally fairly far from the W_o, making the values of f(W_o+W(rhs)) and f(W_o–W(lhs)) nearly equal to F_c. When this happens, the third term exactly cancels with the first, and both are eliminated from the expression.

(2) The absorption lines in ι Her (including the S II line) are fairly symmetric with line asymmetries that are, in general, far below the 7 mÅ observational error. Even when lines are somewhat asymmetric, the effect is usually greatest near the line core and not the local continuum; thus, W(rhs) – W_o equals W_o – W(lhs) even in slightly asymmetric lines. When one deals with a symmetric or nearly symmetric line where W(rhs) – W_o equals W_o – W(lhs), then d(W(lhs))/d(F_c) becomes equal to d(W(rhs))/d(F_c) and f(W_o+W(rhs)) becomes equal to f(W_o–W(lhs)). Thus the first and third terms both tend to be zero.

The above 2 points show that the first and third term tend to be nearly zero, and tend to cancel each other. Because of this, only the second term in the differentiation will be kept giving the following result: $d(W_\lambda) = (1/F_c)(W - W_\lambda)d(F_c)$.

Step 3) The average value of d(W_λ) as the uncertainty.

In general, the uncertainty in the continuum placement depends on whether the continuum is being lowered or raised (i.e. E+ does not equal E–). In general, E+ is dominated by the uncertainty caused by noise at the continuum E+ $\leq F_c$/SNR. The value of E–, on the other hand, is generally more tightly fixed because the lowering of the continuum is easily judged with respect to the depression in flux caused by an absorption line. In order to account for the possibility that E+ is different from E–, one should compute the uncertainty separately for each case.

$$\mathrm{d}(W_\lambda)+ = (\mathrm{E}+/F_c)\ [\ \mathrm{W} - W_\lambda\ ] \text{ and } \mathrm{d}(W_\lambda)- = (\mathrm{E}-/F_c)\ [\ \mathrm{W} - W_\lambda\ ]$$

The final estimate of the uncertainty is the average of d(W_λ)+ and d(W_λ)–, which gives the following.

$$\mathrm{d}(W_\lambda) = (\mathrm{E}/F_c)\ [\ \mathrm{W} - W_\lambda\ ] \text{ where } \mathrm{E} = 0.5\ (\mathrm{E}+ + \mathrm{E}-).$$

This derivation, made independently by the author, is (ignoring photon noise) identical to a result that was derived by Chalabaev and Maillard (1983).

Discussion of the derivation

An important thing to notice about the above derivation is that d(W_λ) depends on the quality (SNR) of the observations. This fact can be seen by considering the smallest value that the uncertainties can take at any point on the continuum; these values correspond to the smallest values that E+ and E– can have. The minimum values of E+ and E– are clearly and directly related the SNR_c of the observations in the following way:

$$\mathrm{E}+ \text{ and } \mathrm{E}- \geq F_c/SNR_c.$$

Because the S II line studied in this thesis is located in a fairly vacant portion of ι Her's spectrum, the uncertainty in the local continuum placement is largely due to noise at the local continuum. This fact, along with the different intrinsic SNR's that exist in the observations at the blue and red regions, require that the uncertainties be studied separately for each of the two regions.

REFERENCES

Abt, H., and Levy, S. 1978, ApJs, **36**, 241.

Belmonte, J.A., Jones, A.R., Palle, P.L., and Roca Cortes, T. 1990, ApJ, **358**, 595.

Chalabaev, A., and Mallard, J.P. 1983, A&A, **127**, 279.

Chapellier, E., Le Contel, J.M., Valtier, J.C., Gonzalez–Bedolla, S., Ducatel, D., Morel, P.J., Sareyan, J.P., Geiger, I., and Antonellie, P. 1987, A&A, **176**, 255.

Cochran, W.D. 1988, ApJ, **334**, 349.

Cox, J.P. 1980, Theory of Stellar Pulsations, Princeton University Press.

Goupil, M.J., and Buchler, J.R. 1994, A&A, **291**, 481.

Hatzes, A.P., and Cochran, W.D. 1993, ApJ, **413**, 339.

Hatzes, A.P., and Cochran, W.D. 1994, ApJ, **422**, 366.

Innis, J.L., Isaak, G.R., Brazier, R.I., Belmonte, J.A., Palle, P.L., Roca Cortes, T., and Jones, A.R. 1988, sess. rept., 569.

Kilian, J., Montenbruck, O., and Nissen, P.E. 1991 A&As, **88**, 101.

Kodaira, K. 1971, Pub. Astr. Soc. Japan, **23**, 159.

Leckrone, D.S. 1971, A&A, **11**, 387.

Lomb, N.R. 1976, Astrophys & SS, **39**, 447.

Mathias, P., and Waelkens, C. 1995, A&A, **300**, 200.

Moore, C.E. 1959, National Bureau of Standards Technical Note No. 36.

Morrison, N.D. 1995, Personal Communication.

Moskalik, P. 1995, in Astrophysical Applications of Stellar Pulsations, eds. R.S. Stobie & P.A. Whitelock, ASP Conference Series Vol 83.

Moskalik, P., and Buchler, J.R., 1994, in Pulsation, Rotation, and Mass Loss in Early–Type Stars, eds. L.A. Balona, H.F. Henrichs, & J.M. Le Contel, IUA Symp. No 162.

Peters, G.J., and Aller, L.H. 1970, ApJ, **159**, 525.

Petrie, R.M., and Petrie, W. 1939, Pub. Dom. Ap. Obs., **7**, 189.

Pintado, O.I., and Adelman, S.J. 1993, MNRAS, **264**, 63.

Rogerson, J.B. Jr 1984, AJ, **89**, 1876.

Sabbey, C.N., Sasselov, D.D., Fieldus, M.S., Lester, J.B., Venn, K.A., and Butler, R.P. 1995, ApJ, **446**, 250.

Sareyan, J.P., Le Contel, J.M., and Valtier, J.C. 1976, A&As, **25**, 129.

Scargle, J.D. 1982, ApJ, **263**, 835.

Shore, S.N., Livio, M., and van den Heuvel, E.P.J. 1994, Interacting Binaries, eds. H. Nussbaumer & A. Orr, Springer–Verlag, New York.

Smith, M.A. 1978, ApJ, **224**, 927.

Smith, M.A. 1981, ApJ, **246**, 905.

Smith, M.A., and Stern, S.A. 1979, AJ, **84**, 1363.

Smith, P.H., McMillan, R.S., and Merline, W.J. 1987, ApJ, **317**, L79.

Sterken, C., Jerzykiewicz, M. 1990, in Confrontation Between Stellar Pulsations and Evolution, eds. C. Cacciari & G. Clementini, ASP Conference Series Vol 11.

Stothers, R. 1972, ApJ, **175**, 431.

Unno, W., Osaki, Y., Ando, H., Saio, H., and Shibahashi, H. 1989, Nonradial Oscillations of Stars: Second Edition, University of Tokyo Press.

Van Hoolst, T. 1994, A&A, **292**, 471.

Waelkens, C. 1991, A&A, **246**, 453.

Wolfe Jr., R.H., Horak, H.G., and Storer, N.W. 1967, in Modern Astrophysics: A memorial to Otto Struve, ed. M. Hack, Gordon And Beach, New York.
